AUTOMATED IMAGE RECONSTRUCTION FOR NON-CARTESIAN MAGNETIC PARTICLE IMAGING

A THESIS SUBMITTED TO

THE GRADUATE SCHOOL OF ENGINEERING AND SCIENCE

OF BILKENT UNIVERSITY

IN PARTIAL FULFILLMENT OF THE REQUIREMENTS FOR

THE DEGREE OF

MASTER OF SCIENCE

IN

ELECTRICAL AND ELECTRONICS ENGINEERING

By

Ali Alper Özaslan

September 2019

Automated Image Reconstruction for Non-Cartesian Magnetic Particle Imaging
By Ali Alper Özaslan
September 2019

We certify that we have read this thesis and that in our opinion it is fully adequate, in scope and in quality, as a thesis for the degree of Master of Science.

Emine Ülkü Sarıtaş Çukur(Advisor)

Tolga Çukur

Nevzat Güneri Gençer

Approved for the Graduate School of Engineering and Science:

Ezhan Karaşan
Director of the Graduate School

ABSTRACT

AUTOMATED IMAGE RECONSTRUCTION FOR NON-CARTESIAN MAGNETIC PARTICLE IMAGING

Ali Alper Özaslan
M.S. in Electrical and Electronics Engineering
Advisor: Emine Ülkü Sarıtaş Çukur
September 2019

Magnetic particle imaging (MPI) is a high-contrast imaging modality that images the spatial distribution of superparamagnetic iron oxide (SPIO) nanoparticles by exploiting their nonlinear response. In MPI, image reconstruction is performed via two different methods: system function reconstruction (SFR) and x-space reconstruction. For the SFR approach, analysis of various scanning trajectories provided important insight about their image quality performances. While Cartesian trajectories remain the most popular choice for x-space-based reconstruction, recent work suggests that non-Cartesian trajectories such as the Lissajous trajectory may prove beneficial for improving image quality. In this thesis, a generalized reconstruction scheme is proposed for x-space MPI that can be used in conjunction with any scanning trajectory. The proposed technique automatically tunes the reconstruction parameters from the scanning trajectory, and does not induce any additional blurring. To demonstrate the proposed technique, five different trajectories were utilized with varying density levels. Comparison to alternative reconstruction methods show significant improvement in image quality achieved by the proposed technique. Among the tested trajectories, the Lissajous and bidirectional Cartesian trajectories prove more favorable for x-space MPI, and the resolution of the images from these two trajectories can further be improved via deblurring. The fully automated gridding reconstruction proposed in this thesis can be utilized with these trajectories to improve the image quality in x-space MPI.

Keywords: Magnetic particle imaging, image reconstruction, gridding reconstruction, non-Cartesian trajectories.

ÖZET

KARTEZYEN OLMAYAN MANYETİK PARÇACIK GÖRÜNTÜLEME İÇİN OTOMATİK GÖRÜNTÜ GERİÇATIMI

Ali Alper Özaslan
Elektrik ve Elektronik Mühendisliği, Yüksek Lisans
Tez Danışmanı: Emine Ülkü Sarıtaş Çukur
Eylül 2019

Manyetik Parçacık Görüntüleme (MPG), süperparamanyetik demir oksit nanoparçacıkların uzaysal dağılımlarını, parçacıkların doğrusal olmayan tepkilerini kullanarak yüksek kontrastla görüntüleyen bir görüntüleme yöntemidir. MPG'de görüntü geriçatımı için iki farklı yöntem kullanılmaktadır: Sistem Fonksiyonu Geriçatımı (SFG) ve x-uzayı geriçatımı. SFG yaklaşımı için çeşitli tarama gezingelerinin analizi, bu gezingelerin görüntü kaliteleri hakkında önemli bilgiler vermiştir. X-uzayı tabanlı geriçatım tekniklerinde ise en çok Kartezyen gezingeler tercih edilirken, son çalışmalar görüntü kalitesini artırmak için Lissajous gibi Kartezyen olmayan gezingelerin kullanılmasının yararlı olabileceğini ortaya koymuştur. Bu tez çalışmasında, x-uzayı tabanlı MPG'nin herhangi bir tarama gezingesiyle birlikte kullanılmasına olanak sağlayacak genel bir geriçatım önerilmektedir. Önerilen teknik, uygulanan tarama gezingesine göre geriçatım parametrelerini otomatik olarak ayarlamakta ve herhangi bir ek bulanıklığa sebep olmamaktadır. Önerilen tekniğin gösterimi amacıyla farklı yoğunluk seviyelerine sahip beş farklı gezinge kullanılmıştır. Alternatif geriçatım teknikleri ile yapılan karşılaştırma, önerilen tekniğin görüntü kalitesini önemli ölçüde artırdığını göstermiştir. Test edilen gezingeler arasında Lissajous ve iki yönlü Kartezyen gezingeleri x-uzayı tabanlı MPG için daha uygundur. Bu iki gezingeden elde edilen görüntülerin çözünürlügü, netleştirme yöntemiyle daha da artırılabilir. Bu tezde önerilen tümüyle otomatik gridleme tabanlı geriçatım yöntemi, bu gezingelerle x-uzayı tabanlı MPG'de görüntü kalitesini artırmak için kullanılabilir.

Anahtar sözcükler: Manyetik parçacık görüntüleme, görüntü geriçatımı, Kartezyen olmayan gezingeler.

Acknowledgement

First of all, I would like to express my gratitudes to my supervisor, Asst. Prof. Emine Ülkü Sarıtaş, for all the support and encouragement she gave me throughout my graduate and undergraduate years. During my undergraduate years, I had a strong interest for academic research and I had a passion for biomedical engineering. I feel very fortunate to meet her during that period of my study and I felt very comfortable working under her supervision because of her positive attitude towards me. Her ambition and dedication for research was always motivational for me. She was always patient and tolerant towards me and always steered me in the right direction whenever I needed. She is a great role model for me and I feel very privileged to have such a supervisor in my academic life.

I would also like to thank Assoc. Prof. Tolga Çukur and Prof. Nevzat Güneri Gençer for being in my thesis committee. I really appreciate their feedbacks and insightful comments on my work.

I would like to thank the following funding agencies for supporting the work in this thesis: the Scientific and Technological Research Council of Turkey through TÜBİTAK Grants 115E677 and 215E198, the Turkish Academy of Sciences through TUBA-GEBIP 2015 program, and the BAGEP Award of the Science Academy.

I would like to thank ASELSAN Healthcare Department for their kindness during the last 6 months of my thesis work. Erdem and Önder made the transition from UMRAM to ASELSAN easier for me.

I would like to thank UMRAM family for providing me a great research environment during my thesis work. I want to thank Bilal Taşdelen, Uğur Yılmaz, Salman Dar, and Emin Çelik for providing me interesting discussions during the times of stress. I would like to thank all former and current members of my research lab: Mustafa Ütkür, Damla Sarıca, Ecem Bozkurt, Çağla Deniz Bahadır, Sevgi Gökçe Kafali, Yavuz Muslu, Burak Demirel, Serhat İlbey, Toygan

Kılıç, Abdullah Ömer Arol, Ecrin Yağız, Rahmetullah Çağıl. They were always helpful and kind to me. Prior to my graduate life, I had the chance the work with Mustafa as an intern and I would like to thank him for introducing me to UMRAM smoothly. I really miss my lunch times with Damla, Ecem, and Çağla during my first graduate year. I want to thank Sevgi and Yavuz for both making either funny or interesting discussions and keeping me focused with their support while I was writing my first journal article, which was pretty hard for me at the beginning. I would like to thank Burak for being really patient to me while he was teaching me background information about my thesis work. Other than academic life, I want to thank Burak for being a healthy cubicle mate and giving me gym and meal tips to become one. I would like to thank Ömer, Ecrin and Rahmi for being great assistantship partners in Industrial Design course and their fruitful discussions on and off the topic.

I am grateful that I started working on this thesis with my friend Ahmet. He was really instrumental in defining the basis for this research. I feel really fortunate to have him both as a friend and a colleague in my life. I would like to thank Koray and Efe for sparing time for me when I needed a break from research. Özgür and Toygan were always there for me and made UMRAM a place that I never want to leave at any time of the day. They spent lots of time with me in UMRAM and thanks to them I had the best moments of my graduate years. I think I could not overcome most of my challenges without them. I would like to thank my best friends Mert, Mehmet and Batuhan for being supportive and cheerful all the time. They always provided me some insight about computer engineering and cleared my head with their funny stories and discussions. I would also like to express my gratitude to Elif Görkem Arslantürk, who was there for me during the most critical stages of my thesis work. With her support, I managed to remain focused and overcome the problems I encountered. I feel very fortunate to have her in my life.

Last but not least, I would like to thank my family for their endless support. They always trusted me and keep me motivated with their support. I would like to thank my mother, Muhterem Özaslan, for providing me moral and emotional support in my life. I would also like to extend thanks to my father, Ali Özaslan, for making me an organized person like him, raising me with a love of science and supporting me in every way. Also, I feel myself very privileged to have a brother like Sarper. Throughout my graduate years, he always provided me happy distractions with his math questions and interesting film and music discussions. This accomplishment would not have been possible without the support of my family, that is why I will always feel grateful to them.

Contents

List of Figures

List of Tables

Chapter 1

Introduction

Magnetic particle imaging (MPI) is a rapidly developing imaging modality that images the spatial distribution of superparamagnetic iron oxide (SPIO) nanoparticles [1–5]. Based on its resolution, sensitivity, and contrast capabilities, MPI promises a wide range of imaging applications such as angiography [6–11], multi-color imaging [12–17], stem cell tracking [18, 19], and functional imaging [20].

There are two main methods for reconstructing an MPI image: system function reconstruction (SFR) and x-space reconstruction. SFR requires a lengthy calibration measurement that records the response from a point-source SPIO sample at all pre-determined pixel locations in the field-of-view (FOV) for a given MPI system and imaging parameters [21–24]. The reconstruction procedure implicitly removes the system and nanoparticle non-idealities to achieve a high-resolution image of the SPIO distribution. X-space reconstruction, on the other hand, models MPI as a linear and shift-invariant (LSI) system that yields an MPI image blurred by a point spread function (PSF) [25–27]. The image is reconstructed by assigning the speed-compensated signal to the instantaneous position of the field free point (FFP). While a calibration scan can completely be omitted with this approach, the blurring effects of the PSF can optionally be deconvolved using a PSF obtained via imaging a point-source SPIO sample. With the LSI assumption, measuring the PSF is a significantly shorter calibration process when compared to the calibration measurement needed for SFR.

For both reconstruction methods, various trajectories can be utilized for scanning the FOV. By far the most popular trajectory used with SFR-based MPI is the Lissajous trajectory [2,6,23,28–30], whereas linear trajectories that raster the FOV approximately line-by-line are most commonly utilized in conjunction with x-space reconstruction [31]. Previously, the performance of different trajectories were evaluated for SFR-based MPI, and compared with the Lissajous trajectory in terms of density, speed, and image quality using a simulation framework [29]. In addition, a simulation study proposed utilizing a radial Lissajous trajectory with SFR, demonstrating improved image quality over the conventional Lissajous trajectory for scanning with overlapping patches [32]. A recent study experimentally compared the Lissajous trajectory and the bidirectional Cartesian trajectory, demonstrating similar results in terms of image quality and sensitivity [33]. For x-space reconstruction, on the other hand, one study suggested that the Lissajous trajectory might improve the overall image resolution within a similar scan time as the linear trajectories [34]. For linear trajectories, it was recently shown that image quality can be improved by scanning the FOV in two orthogonal directions, which helps eliminate the anisotropic blur caused by the PSF [33, 35]. In theory, the same principle should be applicable to other trajectories that feature orthogonal scanning directions, such as the Lissajous trajectory. However, previous studies did not address reconstruction from non-Cartesian trajectory to a Cartesian grid for x-space MPI. Furthermore, an in-depth analysis of trajectories for x-space MPI is currently lacking.

In this thesis, a generalized reconstruction approach is presented for both Cartesian and non-Cartesian trajectories for x-space MPI. The proposed technique is inspired by the gridding algorithms in magnetic resonance imaging (MRI), but includes fundamental modifications to adapt to the reconstruction problems in MPI. Importantly, the proposed technique automatically tunes the two critical reconstruction parameters, kernel width and image size, from the given scanning trajectory. In addition, it does not induce any additional blurring on the MPI image. Here, the proposed technique is demonstrated with simulation results for various non-Cartesian trajectories, including comparison with alternative reconstruction techniques. In addition, the performance of the proposed practical reconstruction model is analyzed on five different non-Cartesian trajectories to infer about their suitability for x-space MPI. The effects of trajectory density and sampling density on image resolution are analyzed, and the performances of additional deblurring techniques are compared to improve the resolution of the gridded x-space MPI images. The proposed method is a trajectory-independent and parameter-free reconstruction scheme, and the results of this thesis provide insight on the suitability of the non-Cartesian trajectories for x-space MPI.

Chapter 2

Magnetic Particle Imaging

2.1 Principles of MPI

Magnetic Particle Imaging (MPI) exploits the nonlinear magnetization of superparamagnetic iron oxide nanoparticles [1]. According to Langevin physics, when the applied magnetic field exceeds a certain threshold, SPIOs are saturated and their magnetization does not change significantly. In an MPI scanner, this saturation property can be exploited by applying an inhomogeneous selection field that generates a field-free point (FFP) and saturates the SPIOs in the remaining imaging volume. Typically, the selection field is generated by permanent magnets with opposing magnetic fields. When a sinusoidal drive field is superimposed to the selection field, SPIOs inside or in the vicinity of the FFP induce a signal on a receive coil, as explained in Figure 2.1. However, if the SPIOs are saturated, they cannot react to the applied drive field and hence cannot induce any signal.

To achieve spatial encoding in MPI, one can steer the FFP and assign the acquired signal to corresponding location of the FFP, which can be calculated from the total magnetic field as follows:

$$H(x,t) = H_d(t) + H_s(x) \tag{2.1}$$

Here, $H_s(x)$ [A/m] is the selection field and is ideally equal to $-Gx$, where G

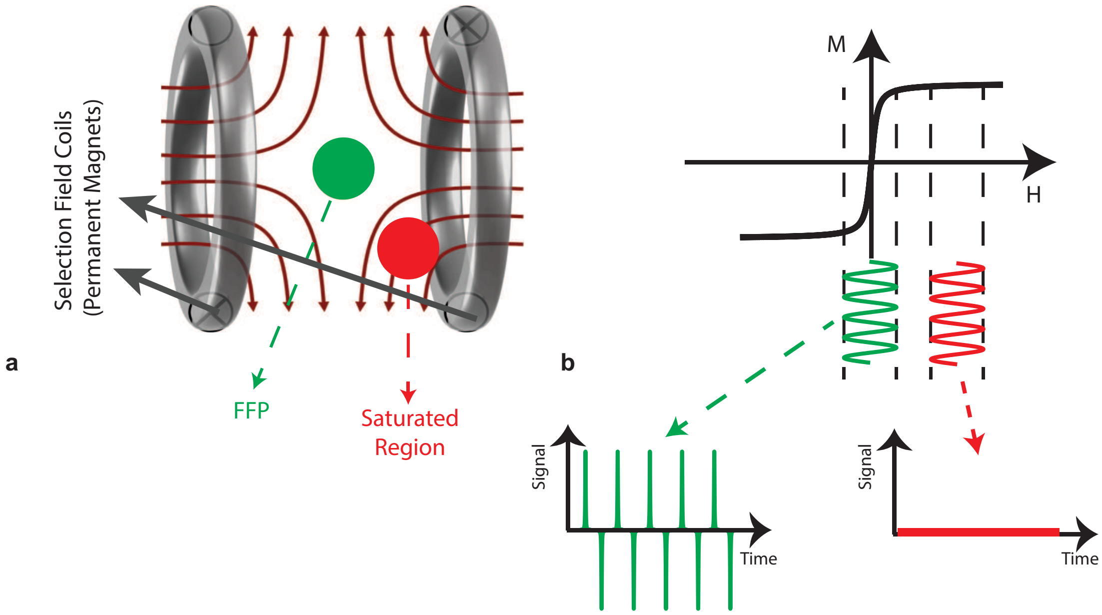

Figure 2.1: **(a)** Generic MPI scanner topology. Here, FFP is denoted with a green circle, while red circle denotes a region where SPIOs are saturated. **(b)** When particles are in the vicinity of the FFP, they induce a signal on the receive coil (green). When particles are saturated by the selection field, they can react to the applied drive field and cannot induce any signal on the receive coil (red).

[A/m/m] is the gradient of the selection field and x [m] is the spatial position. $H_d(t)$ [A/m] is the applied sinusoidal drive field and $H(x,t)$ [A/m] is the total magnetic field [25]. The location of the FFP can be obtained by setting $H(x,t) = 0$. Hence,

$$x_s(t) = \frac{H_d(t)}{G} \tag{2.2}$$

Here, $x_s(t)$ [m] denotes the instantaneous location of the FFP. The magnetization of the nanoparticles can be expressed as a function of the external magnetic field, H, as follows [25]:

$$M = m\rho\mathcal{L}[H/H_{sat}] \tag{2.3}$$

Here, m $[Am^2]$ is the magnetic moment of the nanoparticles, ρ [particles/m^3] is the nanoparticle density, H_{sat} [A/m] is the magnetic field required for saturation, and $\mathcal{L}[\cdot]$ is the Langevin function. For the 1D case, assuming the particle distribution is in x-direction only, the magnetization can be re-written as [25]:

$$M(x,t) = m\rho(x)\delta(y)\delta(z)\mathcal{L}\left[G\left(x_s(t) - x\right)/H_{sat}\right] \tag{2.4}$$

MPI signal can be expressed as follows [25, 36]:

$$s(t) = \int_V B_1 \frac{\partial M(\boldsymbol{x}, t)}{\partial t} dV \tag{2.5}$$

$$= B_1 \frac{\partial}{\partial t} \int_V M(\boldsymbol{x}, t) dV \tag{2.6}$$

where $-B_1$ [T/A] is the sensitivity for the inductive receive coil. Using Eq. 2.6,

$$s(t) = B_1 \frac{\partial}{\partial t} \iiint_S m\rho(u)\delta(v)\delta(\omega)\mathcal{L}\left[G\left(x_s(t) - u\right)/H_{sat}\right] dudvd\omega \tag{2.7}$$

$$= B_1 \frac{\partial}{\partial t} \left(m\rho(x) * \mathcal{L}\left[Gx/H_{sat}\right]\right)\Big|_{x=x_s(t)} \tag{2.8}$$

Finally, the 1D MPI signal can be written as [25]:

$$s(t) = B_1 m\rho(x) * \dot{\mathcal{L}}[Gx/H_{sat}]\Big|_{x=x_s(t)} G\dot{x}_s(t)/H_{sat} \tag{2.9}$$

2.2 Image Reconstruction in MPI

There are two main methods for reconstructing an MPI image: system function reconstruction (SFR) and x-space reconstruction.

2.2.1 System Function Reconstruction (SFR)

SFR method records the MPI signal received from a point-like object placed at all voxel locations inside the imaging volume [21–24]. Hence, SFR approach requires a long calibration process to record the system matrix corresponding to the impulse response of the overall MPI system in Fourier domain. By solving the following inverse problem, one can reconstruct an MPI image using the SFR approach:

$$Sc = u \tag{2.10}$$

Here, S is the system matrix, c is the reconstructed MPI image in vectorized format, and u is the acquired MPI signal in Fourier domain corresponding to the image, c. During the calibration procedure, the Fourier transform of the MPI signal obtained from each voxel in the FOV is placed to the corresponding column of S. This procedure is visualized for a 2D system matrix in Figure 2.2. The solution to the inverse problem given in Eq. 2.10 inherently takes into account system and nanoparticle non-idealities. Thus, the obtained MPI image is not blurred by the PSF of the MPI system.

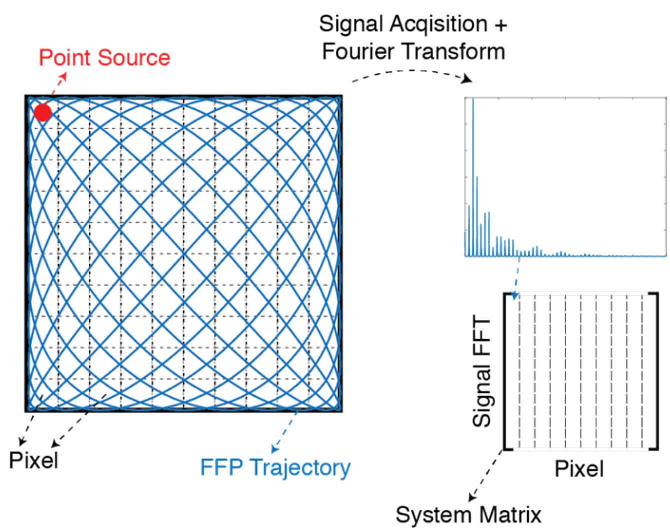

Figure 2.2: Calibration measurements for SFR approach. Point-like source is denoted by red dot, and FFP trajectory is denoted by the blue curve. Once the signal is acquired for a pixel in the FOV, Fourier transform of the signal is placed on the corresponding column of the system matrix. The calibration procedure includes the calibration measurements for all pixels in the FOV.

2.2.2 X-Space Reconstruction

In x-space reconstruction approach, the acquired MPI signal is velocity compensated and gridded to the instantaneous location of the FFP [25–27]. This approach can be expressed as follows:

$$\mathrm{IMG}\left(x_s(t)\right) = \frac{s(t)}{B_1 m G \dot{x}_s(t)/H_{sat}} = \rho(x) * \dot{\mathcal{L}}[Gx/H_{sat}]\Big|_{x=x_s(t)} \tag{2.11}$$

Based on this result, $\dot{\mathcal{L}}[\cdot]$ is the PSF of the imaging system, and $\text{IMG}\,(x_s(t))$ is the MPI image corresponding to the instantaneous location of the FFP. For this approach, a calibration measurement is not needed in the reconstruction stage. However, the reconstructed image is blurred by the PSF of the imaging system.

2.3 Multidimensional X-Space MPI

Derivations given in Sections 2.1 and 2.2.2 can be extended into multidimensional equations using similar physical concepts [26]. For a multidimensional MPI system, the selection field gradient matrix, $\mathbf{G}$, can be expressed as follows:

$$\mathbf{G} = G_{zz}\begin{bmatrix} -\frac{1}{2} & 0 & 0 \\ 0 & -\frac{1}{2} & 0 \\ 0 & 0 & 1 \end{bmatrix} \tag{2.12}$$

Next, a multidimensional drive field can be defined as [26]:

$$\mathbf{H_d}(t) = \begin{bmatrix} H_x(t) \\ H_y(t) \\ H_z(t) \end{bmatrix} \tag{2.13}$$

By using Eqns. 2.12 and 2.13, the total magnetic field is derived as follows [26]:

$$\mathbf{H}(\mathbf{x}, t) = \mathbf{H_d}(t) - \mathbf{G}\mathbf{x} \tag{2.14}$$

$$= \begin{bmatrix} H_x(t) \\ H_y(t) \\ H_z(t) \end{bmatrix} - G_{zz}\begin{bmatrix} -\frac{1}{2} & 0 & 0 \\ 0 & -\frac{1}{2} & 0 \\ 0 & 0 & 1 \end{bmatrix}\begin{bmatrix} x \\ y \\ z \end{bmatrix} \tag{2.15}$$

The instantaneous location of the FFP, $\mathbf{x_s}(t)$, can be found by setting $\mathbf{H}(\mathbf{x}, t)$ to zero [26]:

$$\mathbf{x_s}(t) = \mathbf{G^{-1}}\mathbf{H_d}(t) \tag{2.16}$$

A similar formulation for the magnetization of the SPIOs given in Eq. 2.3, can be preserved while extending it to the multidimensional case [26]:

$$\mathbf{M}(\mathbf{H}) = \rho m \mathcal{L}\left[\frac{||\mathbf{H}||}{H_{sat}}\right]\hat{\mathbf{H}} \tag{2.17}$$

where $\hat{\mathbf{H}} = \mathbf{H}/\|\mathbf{H}\|$. From Eqns. 2.16 and 2.17, magnetization density of the nanoparticles with a distribution of $\rho(\mathbf{x})$ can be written as follows [26]:

$$\mathbf{M}(\mathbf{x},t) = \rho(\mathbf{x})m\mathcal{L}\left[\frac{\|\mathbf{G}\left(\mathbf{x_s}(t)-\mathbf{x}\right)\|}{H_{sat}}\right]\frac{\mathbf{G}\left(\mathbf{x_s}(t)-\mathbf{x}\right)}{\|\mathbf{G}\left(\mathbf{x_s}(t)-\mathbf{x}\right)\|} \tag{2.18}$$

For the case for receive coils in x,y, and z axes, sensitivity matrix can be defined as $-\mathbf{B_1}(\mathbf{x}) = [\mathbf{B_{1x}}(\mathbf{x})\ \mathbf{B_{1y}}(\mathbf{x})\ \mathbf{B_{1z}}(\mathbf{x})]^T$. Then, multidimensional signal equation can be obtained as follows [26]:

$$s(t) = \frac{d}{dt}\iiint \mathbf{B_1}(\mathbf{u})\mathbf{M}(\mathbf{u},t)d\mathbf{u} \tag{2.19}$$

With some simplifications applied on Eq. 2.19 [26] (see Appendix A), the following multidimensional signal equation, which is the three-dimensional extension of Eq. 2.9, can be written [26]:

$$s(t) = \mathbf{B_1}(\mathbf{x})m\rho(\mathbf{x}) *** \frac{\|\dot{\mathbf{x}}_\mathbf{s}\|}{H_{sat}}\mathbf{h}(\mathbf{x})\hat{\dot{\mathbf{x}}}_s\bigg|_{\mathbf{x}=\mathbf{x_s}(t)} \tag{2.20}$$

Here, $\hat{\dot{\mathbf{x}}}_s$ represents the scanning direction and $\mathbf{h}(\mathbf{x})$ is the PSF [26]:

$$h(\mathbf{x}) = \dot{\mathcal{L}}\left(\frac{\|\mathbf{Gx}\|}{H_{\text{sat}}}\right)\frac{\mathbf{Gx}}{\|\mathbf{Gx}\|}\left[\frac{\mathbf{Gx}}{\|\mathbf{Gx}\|}\right]^T\mathbf{G} + \frac{\mathcal{L}\left(\frac{\|\mathbf{Gx}\|}{H_{\text{sat}}}\right)}{\frac{\|\mathbf{Gx}\|}{H_{\text{sat}}}}\left(\mathbf{I} - \frac{\mathbf{Gx}}{\|\mathbf{Gx}\|}\left[\frac{\mathbf{Gx}}{\|\mathbf{Gx}\|}\right]^T\right)\mathbf{G} \tag{2.21}$$

The PSF can be decomposed into two envelopes, the tangential and normal envelopes [26]:

$$ENV_T = \dot{\mathcal{L}}\left(\frac{\|\mathbf{Gx}\|}{H_{\text{sat}}}\right) \tag{2.22}$$

$$ENV_N = \frac{\mathcal{L}\left(\frac{\|\mathbf{Gx}\|}{H_{\text{sat}}}\right)}{\frac{\|\mathbf{Gx}\|}{H_{\text{sat}}}} \tag{2.23}$$

As displayed in Figure 2.3, the tangential envelope is significantly narrower than the normal envelope. The full-width at half-maximum (FWHM) values for the envelopes can be approximated as 4.2 and 9.5 for the tangential and normal envelopes, respectively [26]. In 3-D x-space MPI theory, the images are produced on an internal reference frame formed by two vectors that are collinear and transverse to the FFP velocity vector [26]. For example, if $\dot{x}_s$ is aligned with

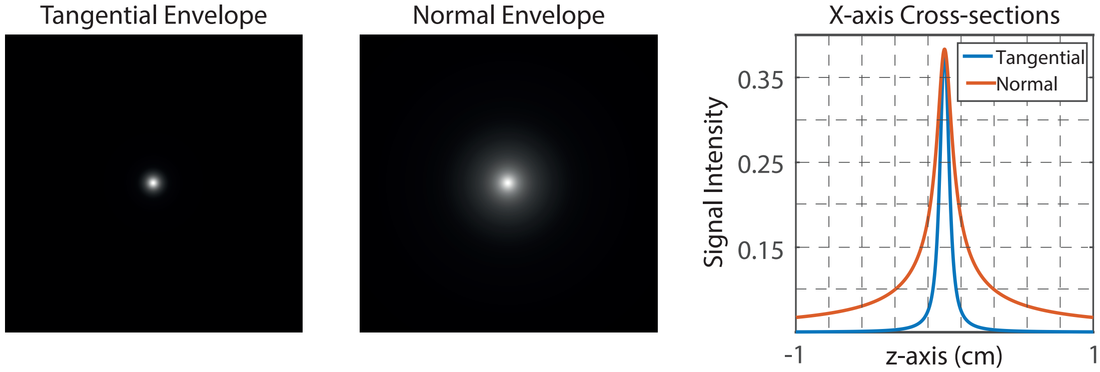

Figure 2.3: **(a)** Tangential and Normal Envelopes for $G = 3$ T/m/μ_0. **(b)** X-axis cross sections of both envelopes. The tangential envelope is significantly narrower than the normal envelope.

the x-axis, the collinear and transverse components of the PSF can be written as follows:

$$\mathrm{h}_{\|}(\mathbf{x}) = \hat{\mathbf{e}}_{\mathbf{1}} \cdot \mathbf{h}(\mathbf{x})\hat{\mathbf{e}}_{\mathbf{1}} \quad \text{collinear} \tag{2.24}$$

$$\mathrm{h}_{\perp,1}(\mathbf{x}) = \hat{\mathbf{e}}_2 \cdot \mathbf{h}(\mathbf{x})\hat{\mathbf{e}}_{\mathbf{1}} \quad \text{transverse} \tag{2.25}$$

$$\mathrm{h}_{\perp,2}(\mathbf{x}) = \hat{\mathbf{e}}_3 \cdot \mathbf{h}(\mathbf{x})\hat{\mathbf{e}}_{\mathbf{1}} \quad \text{transverse} \tag{2.26}$$

Here, $\hat{\mathbf{e}}_1$, $\hat{\mathbf{e}}_2$, and $\hat{\mathbf{e}}_3$ are the unit vectors in x, y, and z axes, respectively. Finally, the collinear and transverse components of the PSF for this case can be expressed as follows [26]:

$$h_{\|}(x,y,z) = \dot{\mathcal{L}}\left(\frac{H(x,y,z)}{H_{sat}}\right)\frac{G_{zz}^3 z^2}{H(x,y,z)^2} + \frac{\mathcal{L}\left(\frac{H(x,y,z)}{H_{sat}}\right)}{\frac{H(x,y,z)}{H_{sat}}} G_{zz}\left(1 - \frac{G_{zz}^2 z^2}{H(x,y,z)^2}\right)$$

$$h_{\perp}(x,y,z) = \dot{\mathcal{L}}\left(\frac{H(x,y,z)}{H_{sat}}\right)\frac{G_{xx}G_{zz}^2 xz}{H(x,y,z)^2} - \frac{\mathcal{L}\left(\frac{H(x,y,z)}{H_{sat}}\right)}{\frac{H(x,y,z)}{H_{sat}}} \frac{G_{xx}G_{zz}^2 xz}{H(x,y,z)^2}$$

where $H(x,y,z) = \sqrt{(G_{xx}x)^2 + (G_{yy}y)^2 + (G_{zz}z)^2}$. The collinear PSF, $h_{\|}(x,y,z)$, is the vector sum of the tangential and normal envelopes and it forms the desired resolution. However, the transverse PSF, $h_{\perp}(x,y,z)$, is the vector difference of two envelopes and its magnitude is much smaller than that of the collinear PSF. (see Figure 2.4) [26].

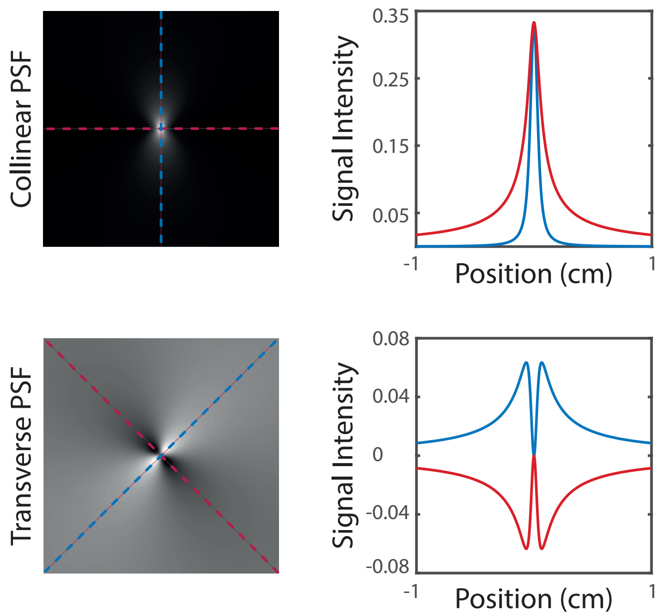

Figure 2.4: Collinear and transverse components of the PSF for $G = 3$ T/m/μ_0.. These components depend on the scanning direction. The collinear component has higher peak amplitude than the transverse component.

Chapter 3

Theory

Among the two components of the PSF shown in Figure 3.1a, the collinear component is narrower and better behaved. Hence, this component has the capability to provide a higher resolution and higher quality MPI image [26], as shown in Figure 3.1c. One method to capture only the collinear component is to align the axis of the receive coil with the FFP velocity vector. This method is straightforward when the drive field is in one direction only, e.g., a drive field in the z-direction together with a single-channel receive coil sensitive along that direction. For multi-dimensional drive fields, a more practical approach is to use multiple receive coils and combine their signals to form a virtual receive coil aligned with the instantaneous FFP velocity vector [37]. In the following sections, extraction process of the collinear image component is briefly described and then followed by a detailed explanation of the proposed gridding algorithm. The derivations assume ideal magnetic fields and measurements, and instantaneous alignment of the nanoparticle magnetization with the applied field. The proposed technique builds on the mathematical basis and fundamental steps of the original x-space reconstruction (i.e., speed compensation and assigning the data to instantaneous FFP position) [25, 26], while extending it to more complicated multi-dimensional trajectories.

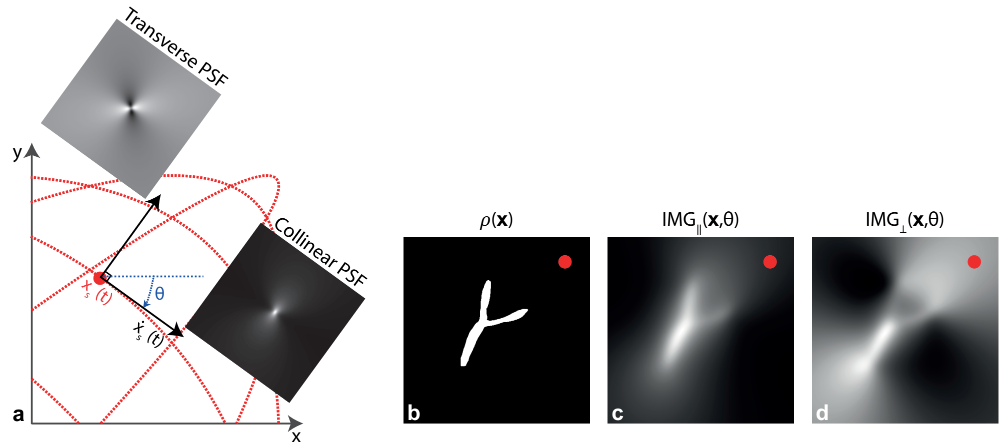

Figure 3.1: The collinear and transverse image components for x-space MPI. **(a)** The collinear and transverse PSFs for x-space MPI, rotated at an angle θ to align with the instantaneous velocity vector. Here, the FFP is following a Lissajous trajectory in x-y plane (displayed in zoomed format). **(b)** The nanoparticle distribution in space. **(c)** The collinear image and **(d)** the transverse image, i.e., the convolutions of the nanoparticle distribution with the collinear and transverse PSFs at angle θ, respectively. The red dot denotes the instantaneous position of the FFP.

3.1 Extraction of Collinear Image Components

Assuming a 2D FFP trajectory in x-y plane (e.g., 2D Lissajous) together with two receive coils aligned in the physical x- and y-directions, the signals induced on the receive coils can be expressed as [26]:

$$s_x(t) = B_{1,x} m \frac{\|\dot{\mathbf{x}}_\mathbf{s}(t)\|}{H_{sat}} \{IMG_\parallel\left(\mathbf{x_s}(t), \theta(t)\right) \cos(\theta(t)) - IMG_\perp\left(\mathbf{x_s}(t), \theta(t)\right) \sin(\theta(t))\} \tag{3.1a}$$

$$s_y(t) = B_{1,y} m \frac{\|\dot{\mathbf{x}}_\mathbf{s}(t)\|}{H_{sat}} \{IMG_\parallel\left(\mathbf{x_s}(t), \theta(t)\right) \sin(\theta(t)) + IMG_\perp\left(\mathbf{x_s}(t), \theta(t)\right) \cos(\theta(t))\} \tag{3.1b}$$

where,

$$IMG_\parallel\left(\mathbf{x_s}(t), \theta(t)\right) = \rho(\mathbf{x}) * h_\parallel\left(\mathbf{x}, \theta(t)\right)\big|_{\mathbf{x}=\mathbf{x_s}(t)} \tag{3.2a}$$

$$IMG_\perp\left(\mathbf{x_s}(t), \theta(t)\right) = \rho(\mathbf{x}) * h_\perp\left(\mathbf{x}, \theta(t)\right)\big|_{\mathbf{x}=\mathbf{x_s}(t)} \tag{3.2b}$$

Here, $\theta(t)$ is the angle of the FFP velocity vector with respect to the x-axis, $h_{\parallel}(\mathbf{x}, \theta(t)))$ and $h_{\perp}(\mathbf{x}, \theta(t)))$ are the collinear and transverse PSFs, rotated by angle θ to align with the direction of the FFP velocity vector at time t, as demonstrated in Figure 3.1a. Next, $IMG_{\parallel}(\mathbf{x_s}(t), \theta(t))$ and $IMG_{\perp}(\mathbf{x_s}(t), \theta(t))$ are the collinear and transverse images as a function of FFP position at time t, as shown in Figure 3.1c and Figure 3.1d. These images correspond to the nanoparticle distribution convolved with the collinear and transverse PSFs at time t, respectively. As seen in this figure, the collinear image displays significantly better image quality and resolution than the transverse image. Furthermore, the collinear image has better resolution along the direction of the FFP velocity vector when compared to the orthogonal direction.

The first goal is to extract only the collinear image component from the signals $s_x(t)$ and $s_y(t)$. For this purpose, the signal for a virtual receive coil aligned with the FFP velocity vector can be computed as [37]:

$$
\begin{aligned}
s_v(t) &= \frac{s_x(t)}{B_{1,x}} \cos(\theta(t)) + \frac{s_y(t)}{B_{1,y}} \sin(\theta(t)) && \text{(3.3a)} \\
&= m \frac{\|\dot{\mathbf{x}}_\mathbf{s}(t)\|}{H_{sat}} IMG_{\parallel}(\mathbf{x_s}(t), \theta(t)) && \text{(3.3b)}
\end{aligned}
$$

As mentioned in Section 2.2.2, a fundamental step in x-space reconstruction is to compensate the received signal by the FFP speed [25, 26]. For the virtual coil, the resulting image as a function of time can then be expressed as:

$$
IMG_v(\mathbf{x_s}(t)) = \frac{s_v(t)}{\|\dot{\mathbf{x}}_\mathbf{s}(t)\|} = \alpha IMG_{\parallel}(\mathbf{x_s}(t), \theta(t)) \tag{3.4}
$$

Here, $\alpha = m/H_{sat}$ is a constant. As seen in this expression, the image from the virtual coil captures only the desired collinear component of the MPI image. In the proposed reconstruction described below, only this component is gridded to achieve a higher quality x-space MPI image.

3.2 Gridding for X-space MPI

In the literature, gridding algorithms were originally proposed for the reconstruction of MRI images that utilize non-Cartesian k-space trajectories, such as radial or spiral trajectories [38, 39]. These non-Cartesian trajectories provide several advantages such as motion robustness [40, 41], and fast data acquisition and efficient coverage of k-space [42, 43]. In MRI gridding reconstruction, data points lying on a non-Cartesian k-space trajectory are first convolved with a kernel, and the outcome of the convolution operation is sampled and accumulated onto a Cartesian k-space grid. After density compensation of the scanning trajectory, an MRI image is produced using inverse Fourier transform, followed by apodization correction in image domain [44, 45].

As opposed to MRI gridding algorithms that operate in k-space, the reconstruction in x-space MPI is performed directly in image domain. Here, following gridding algorithm is proposed for x-space image reconstruction in MPI:

$$I\hat{M}G(\mathbf{x}) = \frac{I\hat{M}G_{init}(\mathbf{x})}{\hat{d}_s(\mathbf{x})} = \frac{((IMG(\mathbf{x})s(\mathbf{x})) * c(\mathbf{x})) \cdot \text{III}\left(\frac{\mathbf{x}}{\Delta x}\right)}{(s(\mathbf{x}) * c(\mathbf{x})) \cdot \text{III}\left(\frac{\mathbf{x}}{\Delta x}\right)} \tag{3.5}$$

where,

$$s(\mathbf{x}) = \sum_{i=1}^{N_s} \delta\left(\mathbf{x} - \mathbf{x}_i\right) \tag{3.6a}$$

$$IMG(\mathbf{x_i}) = IMG_v\left(\mathbf{x_s}(t_i)\right), \text{ for } i = 1, \ldots, N_s \tag{3.6b}$$

Here, $s(\mathbf{x})$ is a non-Cartesian sampling function composed of impulses placed at sampled FFP locations, $\mathbf{x_i} = \mathbf{x_s}(t_i)$. $IMG(\mathbf{x})$ denotes the entire image that is desired to be reconstructed with values only known at sampled FFP locations, where they are equal to $IMG_v\left(\mathbf{x_s}(t)\right)$. In addition, $c(\mathbf{x})$ is the gridding kernel in x-space, $\text{III}\left(\frac{\mathbf{x}}{\Delta x}\right)$ is a 2D Comb function used for re-sampling onto the Cartesian

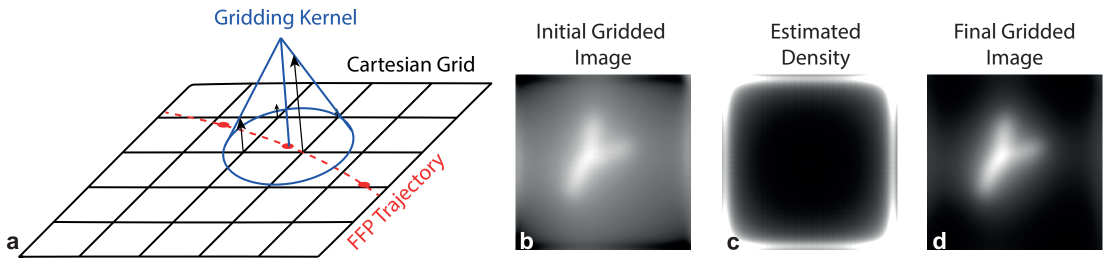

Figure 3.2: The proposed gridding algorithm. **(a)** Each data point on the FFP trajectory is convolved with the gridding kernel and re-sampled onto a Cartesian grid. **(b)** The initial gridded image is over-amplified at locations where the trajectory is dense. **(c)** The estimated density of the FFP trajectory. **(d)** The final gridded image is obtained via dividing the initial gridded image by the estimated density. A Lissajous trajectory was used in this example.

grid, Δx is the spatial distance between neighboring Cartesian grid points (i.e., the resolution of the grid, assumed to be the same for x- and y-directions), and N_s is the total number of acquired samples.

As visualized in Figure 3.2a, the steps of the proposed gridding algorithm can be explained as follows. First, the MPI signal is obtained by scanning the FOV with an FFP trajectory, followed by the virtual coil alignment step, as described in Eqns. (3.1)-(3.3). The collinear component of the MPI image, $IMG_v\left(\mathbf{x_s}(t)\right)$, is then captured as a function of FFP position as given in Eq. (3.4), which forms the sampled data, $IMG(\mathbf{x})s(\mathbf{x})$. Then, each data point on the non-Cartesian trajectory is convolved with the gridding kernel, $c(\mathbf{x})$, and re-sampled onto the Cartesian grid using the 2D Comb function, $Ш\left(\frac{\mathbf{x}}{\Delta x}\right)$. This initial gridded image, $I\hat{M}G_{init}(\mathbf{x})$, is over-amplified at locations where the trajectory is dense (see Figure 3.2b). As shown in Figure 3.2c, an estimate of the trajectory density, $\hat{d}_s$, can be computed by gridding ones (i.e., using $IMG(\mathbf{x}) = 1$). Dividing the initial gridded image by the density provides the density compensated image, $I\hat{M}G(\mathbf{x})$, which is the final reconstructed x-space MPI image (see Figure 3.2d).

For the gridding kernel, a Kaiser-Bessel window is used, which is a popular choice in MRI gridding algorithms [45]. This kernel can be expressed as:

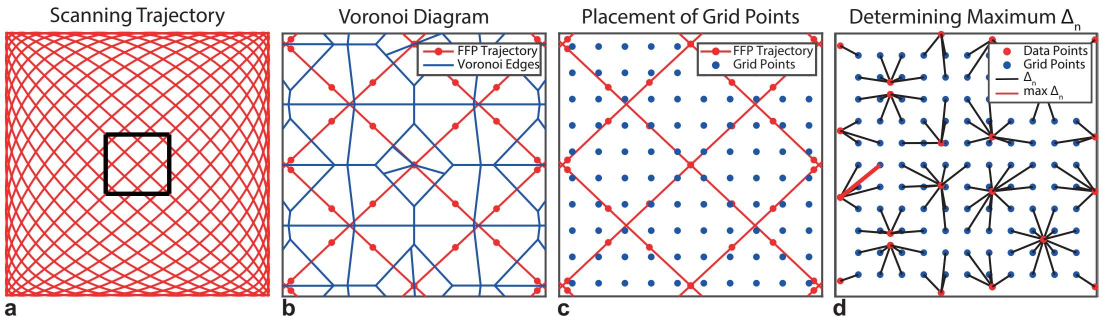

Figure 3.3: The proposed steps for tuning the kernel width and grid size directly from the FFP trajectory. **(a)** An example Lissajous trajectory with a frequency ratio of 17/16. The subsequent subfigures zoom in on the region marked with the black box. **(b)** A Voronoi diagram is used to calculate the areas associated with each data point on the FFP trajectory. The grid size, N, is computed using the effective edge sizes from all partitions. **(c)** $N \times N$ Cartesian grid points are placed on the FOV. **(d)** For each grid point, the distance to the nearest data point, Δ_n, is computed. The optimal kernel width is chosen as a multiple of the maximum Δ_n.

$$c(\mathbf{x}) = I_0\left(\beta\sqrt{1-\left(\frac{2\left\|\mathbf{x}\right\|}{w_k \Delta x}\right)^2}\right) \tag{3.7}$$

where,

$$\Delta x = \frac{x_{FOV}}{N} \tag{3.8}$$

Here, I_0 is the zero-order modified Bessel function of the first kind, x_{FOV} is the extent of the FOV (assumed to be identical in x- and y-directions to simplify the notations), N is the reconstructed image size (i.e., corresponding to an $N \times N$ image for the case of 2D imaging), w_k is the full kernel width in grid units, and β denotes the shape parameter of the Kaiser-Bessel kernel. In MRI, β is chosen as a function of w_k to carefully place the zero crossings of the inverse 2DFT of the gridding kernel at the edge of the stopband. In MPI, since $c(\mathbf{x})$ operates directly in image domain, thus it is not a concern. The choice of β for the proposed algorithm is explained in the following section.

3.3 Automated Tuning of Gridding Parameters

There are fundamental differences between MRI gridding algorithms and the proposed x-space MPI gridding algorithm. First, while MRI gridding algorithms can leave certain k-space locations unfilled, the gridding in x-space MPI must spread the acquired data to all pixels on the Cartesian image grid. Secondly, the resolution of an MRI image is directly dictated by the extent of the acquired k-space, which in turn determines the image size. In contrast, there is no strict information that determines the image size or grid resolution in x-space MPI. Therefore, the kernel width (w_k) and image size (N) parameters require careful tuning to achieve high-quality x-space MPI images via the proposed technique. Here, these important parameters are computed automatically from the FFP trajectory, without manual intervention.

For computing the image size, a plane-partitioning method called Voronoi diagram is utilized. Voronoi diagrams have been utilized extensively for determining the sampling density of scanning trajectories in MRI and computed tomography (CT) [46]. In MPI also, Voronoi diagrams were utilized to determine the areas associated with the node points of the Lissajous trajectory, to be used as weights in SFR for reconstructing an image at these nodes [47]. In the proposed method, Voronoi diagram is utilized for a different purpose: for determining an optimal image size directly from the trajectory data points.

Figure 3.3 illustrates the computation of N and w_k for the case of a Lissajous trajectory. In Figure 3.3b, the Voronoi diagram divides the FOV into sub-regions by bisecting the connections between each data point and its closest neighbors, which are determined using Delaunay triangulation [46]. Following bisection, each data point is associated with a sub-region, called the Voronoi partition. For each data point on the scanning trajectory, the area associated with its partition is computed. To prevent infinitely large partitions for data points near the periphery of the trajectory, the trajectory is first surrounded by external dummy data points. Depending on the bounded shape of the scanning trajectory, these dummy data points traverse a rectangle or a circle that surrounds the trajectory.

After the computation of the areas for all Voronoi partitions, the dummy points are excluded from consideration.

Using the Voronoi partitions, the image size is determined as follows:

$$N = \left[\frac{1}{N_s} \sum_{i=1}^{N_s} \frac{x_{FOV}}{d_{V,i}} \right] = \left[\frac{1}{N_s} \sum_{i=1}^{N_s} \frac{x_{FOV}}{\sqrt{A_{V,i}}} \right] \tag{3.9}$$

Here, $[\cdot]$ denotes the rounding operation and $A_{V,i}$ is the area of the Voronoi partition corresponding to the i^{th} data point. Here, it is proposed that the Voronoi partition for each data point dictates the effective pixel size around that point. Approximating each Voronoi partition as a square region, $d_{V,i} = \sqrt{A_{V,i}}$ yields the effective edge size for the i^{th} Voronoi partition. This edge size is considered to be the local pixel size associated with the i^{th} data point. Next, a corresponding image size is computed via dividing FOV by this edge size. Finally, the mean over all data points is computed to reach the final image size, N. The corresponding pixel size for the Cartesian grid, Δx, can then be computed using Eq. (3.8). Following the aforementioned steps, $N \times N$ Cartesian grid points can be positioned in space, as shown in Figure 3.3.

To tune the kernel width, w_k, it should be assured that the kernel should be sufficiently wide to ensure that no grid points are left unfilled after gridding, but not overly wide to induce unnecessary image blurring. First, for each grid point in the image, the distance to the nearest data point is calculated as follows:

$$\Delta_n = \min_{i \in 1:N_s} \frac{\|\mathbf{x_n} - \mathbf{x_i}\|}{\Delta x} \tag{3.10}$$

Here, $\mathbf{x_i}$ is the location of the i^{th} data point, $\mathbf{x_n}$ is the location of the n^{th} grid point, and Δ_n is the distance in grid units between the n^{th} grid point and the nearest data point. This operation is performed for each grid point, as shown in Figure 3.3d. Next, the kernel width is chosen as a multiple of the maximum Δ_n, i.e.

$$w_k = \gamma \cdot \max_{n \in \Omega^2} \Delta_n \tag{3.11}$$

Here, Ω^2 denotes the image grid and γ is a constant to ensure that w_k is sufficiently large to spread not just one but multiple data points to each grid point. This constant was determined based on two factors: quantitative image quality assessment via the PSNR metric (see Methods section for the definition) and visual inspection. The results of the PSNR assessment are given in Figure 3.4a for the Lissajous trajectory at $N_p = 98$ with a sampling factor of 1. The phantom used in this assessment is displayed in Figure 3.4b together with the results of the gridding algorithm at various γ values. The PSNR assessment implies that higher γ values result in reduced image quality, with $\gamma = 3$ yielding the highest PSNR. However, the corresponding image visibly suffers from vertical stripe artifacts (shown by red arrows), which are remnants of the scanning trajectory. As γ increases, the intensity of this artifact weakens and finally disappears for γ greater than 5-6. On the other hand, a higher γ value directly corresponds to a higher $FWHM_k$, causing an increased blurring in the reconstructed image. The PSNR metric successfully captures this reduction in resolution for higher γ values, but fails to detect the artifacts seen at lower γ values. To prevent such artifacts while preserving the resolution of the reconstructed images, $\gamma = 6$ is chosen, which is the smallest integer-valued γ that yields artifact-free images.

Finally, the shape parameter, β, for the Kaiser-Bessel window given in Eq. (3.7) is chosen. This parameter is chosen to ensure that: (1) the full kernel width, w_k, tightly covers the full shape of the Kaiser-Bessel window, and (2) the full width at half maximum (FWHM) of the kernel, $FWHM_k$, is equal to half the kernel width, i.e.,:

$$FWHM_k \approx \frac{w_k}{2} \Delta x \tag{3.12}$$

Both of these criteria are satisfied for $\beta = 6$, which provides an efficient representation of the gridding kernel as shown in Figure 3.5.

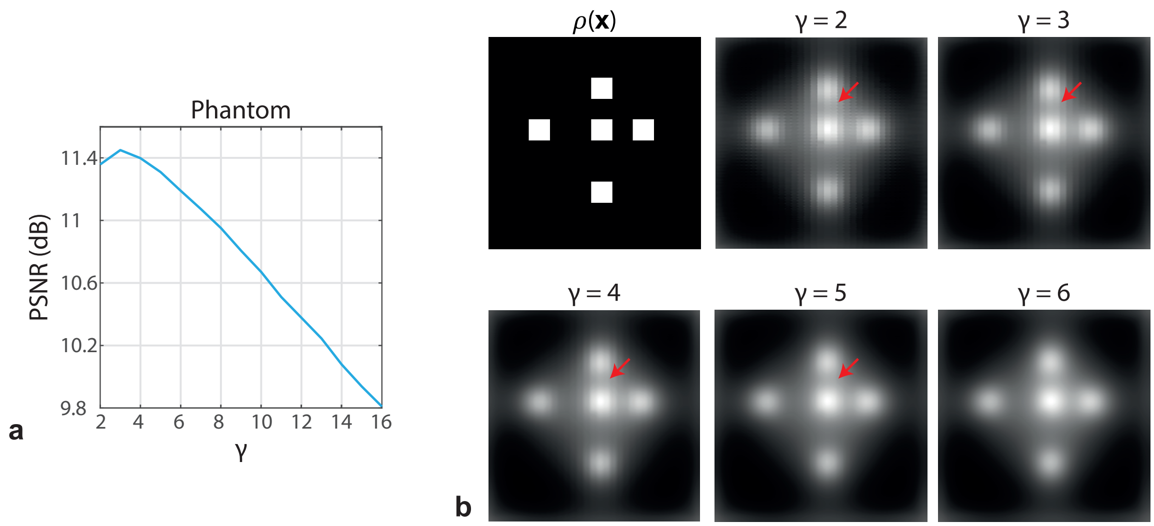

Figure 3.4: The effect of γ on image quality. **(a)** PSNR analysis indicates that highest image quality is achieved at $\gamma = 3$, with higher γ values causing a reduction in image quality. **(b)** The phantom and the results of the gridding algorithm for various γ values. Vertical stripe artifacts not captured by the PSNR metric are clearly visible in the reconstructed image for $\gamma = 3$ (red arrow). These artifacts diminish at higher γ values, however, the image resolution also worsens simultaneously. Here, the choice of $\gamma = 6$ corresponds to the smallest integer-valued γ that yields artifact-free images.

3.4 Deblurring of Reconstructed Images

The resulting images from the gridding algorithm are blurred by the collinear and transverse PSFs. Here, to improve the resolution of the reconstructed images, an optional post-processing step can be performed following the gridding reconstruction. Two candidate methods for deblurring the images are the equalization filter [48, 49] and Wiener deconvolution.

The equalization filter is a k-space filter inspired by the ramp filter in computed tomography (CT), which is used to eliminate the background haze due to overemphasis of the low-frequency data resulting from projections. In x-space MPI, a similar overemphasis of low spatial frequencies occurs due to the wide "normal envelope" component of the PSFs. The equalization filter was originally proposed for multichannel acquisitions where two separate images are acquired

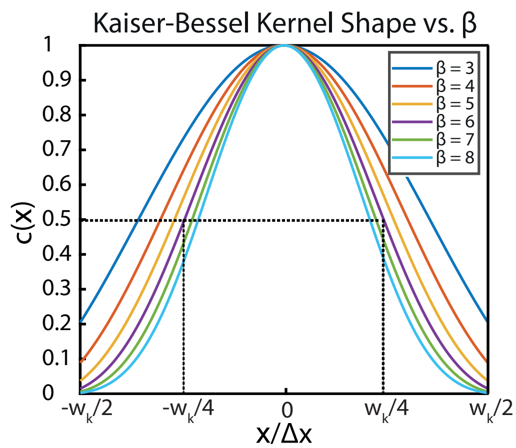

Figure 3.5: The shape of the Kaiser-Bessel window depends on the shape parameter β. When $\beta = 6$ (purple line), the Kaiser-Bessel window tightly covers the full kernel width and its FWHM is approximately equal to $w_k/2$ in grid units.

using a single-channel drive field that is 90° rotated during the second acquisition. These two images are then averaged, resulting in an isotropic blur with the following effective PSF:

$$h_{iso}(\mathbf{x}) = h_{\|}(\mathbf{x}, 0^\circ) + h_{\|}(\mathbf{x}, 90^\circ) \tag{3.13}$$

It was previously shown that this PSF can also be expressed as $E_T(\mathbf{x}) + 2E_N(\mathbf{x})$ [35, 50], where $E_T(\mathbf{x})$ and $E_N(\mathbf{x})$ are the tangential and the normal envelopes of the PSFs as defined in [26]. The equalization filter aims to eliminate image haze by decomposing the effective PSF into its tangential and normal components, and extracting the narrower tangential component only. This filter is applied to the reconstructed MPI images in k-space (i.e., multiplied with the Fourier transform of the image, followed by inverse Fourier transformation). For multichannel acquisition, this filter is formulated as [49]:

$$\Phi_{eq}(\mathbf{k}) = \frac{\mathcal{F}\left(E_T(\mathbf{x})\right)}{\mathcal{F}\left(E_T(\mathbf{x}) + 2E_N(\mathbf{x})\right)} \tag{3.14}$$

where $\mathcal{F}$ is the Fourier transform operator. It should be noted that equalization does not aim to fully deconvolve the effects of the imaging PSF. Instead, as seen in Eq. (3.14), the goal is to improve the effective PSF from $E_T(\mathbf{x}) + 2E_N(\mathbf{x})$ to $E_T(\mathbf{x})$. In contrast to standard deconvolution filters, this filter does not cause division by zero problems at high spatial frequencies where the SNR is typically low.

The equalization filter can potentially be suitable for the Lissajous and bidirectional Cartesian trajectories, as they are composed of two approximately orthogonal scanning directions. For these trajectories, the overall PSF of the imaging system can be heuristically approximated as $h_{iso}(\mathbf{x})$ [51]. Following a similar idea, this PSF can also be utilized for Wiener deconvolution. The corresponding Wiener deconvolution filter in k-space can then be formulated as follows:

$$G_w(\mathbf{k}) = \frac{{H_{iso}}^*(\mathbf{k})}{\mid H_{iso}(\mathbf{k}) \mid^2 + NSR} \tag{3.15}$$

Here, $H_{iso}(\mathbf{k})$ is the Fourier transform of $h_{iso}(\mathbf{x})$, * denotes the conjugation operation, and NSR is the noise-power-to-signal-power ratio, added to the denominator to avoid excessive noise amplification.

Chapter 4

Materials and Methods

4.1 Trajectories

In this thesis, the proposed gridding algorithm is applied to five non-Cartesian trajectories, as illustrated in Figure 4.1: Lissajous, bidirectional Cartesian, radial Lissajous, spiral, and radial trajectories. The mathematical expressions for the trajectories are given in 4.1. The choice of trajectories was guided by an earlier trajectory analysis work on SFR-based MPI [29, 32], with the addition of the radial Lissajous trajectory. Considering hardware feasibility of the bidirectional Cartesian trajectory, a modification was performed over the theoretical version presented in 4.1: the abrupt switch that occurs at multiples of half-period time points were smoothed to reach a more realistic trajectory in terms of hardware constraints, as shown in Figure 4.1. Among the tested trajectories, only the Lissajous trajectory have been utilized in existing MPI hardware. The bidirectional Cartesian trajectory was only utilized as two orthogonal linear acquisitions [33, 35], and not as shown in Figure 4.1.

The important parameters in Table 4.1 are the fundamental drive field frequency, f_0, and the trajectory density parameter, N_P. The parameter N_P determines the frequency ratio between the two orthogonal drive channels. For all five

Table 4.1: The mathematical expressions for the non-Cartesian FFP trajectories used in this thesis. The 2D drive fields and frequency ratios to generate the corresponding trajectories are given. f_0 is the fundamental drive field frequency, N_P is the trajectory density parameter, and $T_R = N_P/f_0$ is one period of the trajectory. A and B correspond to the drive field amplitudes in x- and y-directions, respectively.

Trajectories	Mathematical Expression	Frequency Ratio
Lissajous	$H_x(t) = A\sin(2\pi f_0 t)$ $H_y(t) = B\sin(2\pi f_1 t + \phi)$	$f_0 = \frac{N_P}{N_P - 1} f_1$
Bidirectional Cartesian	$H_x(t) = \begin{cases} A\sin(2\pi f_0 t), & t < \frac{T_R}{2} \\ B\sin(2\pi f_1 t + \phi), & t \geq \frac{T_R}{2} \end{cases}$ $H_y(t) = \begin{cases} A\sin(2\pi f_1 t + \phi), & t < \frac{T_R}{2} \\ B\sin(2\pi f_0 t), & t \geq \frac{T_R}{2} \end{cases}$	$f_0 = \frac{N_P}{2} f_1$
Spiral	$H_x(t) = A\sin(2\pi f_1 t) \cdot \cos(2\pi f_0 t)$ $H_y(t) = B\sin(2\pi f_1 t) \cdot \sin(2\pi f_0 t)$	$f_0 = N_P f_1$
Radial Lissajous	$H_x(t) = A\sin(2\pi f_0 t) \cdot \sin(2\pi f_1 t)$ $H_y(t) = B\sin(2\pi f_1 t) \cdot \cos(2\pi f_0 t)$	$f_0 = \frac{N_P}{N_P - 1} f_1$
Radial	$H_x(t) = A\sin(2\pi f_0 t) \cdot \sin(2\pi f_1 t)$ $H_y(t) = B\sin(2\pi f_1 t) \cdot \cos(2\pi f_0 t)$	$f_0 = N_P f_1$

trajectories listed, larger N_P values result in a denser FFP trajectory.

4.2 Simulations

The simulations were performed on a custom MPI toolbox developed in MATLAB (Mathworks, Natick, MA). The performance of the proposed gridding algorithm

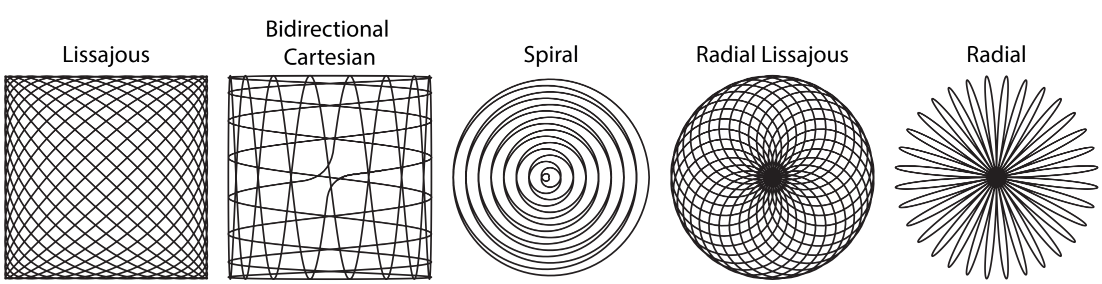

Figure 4.1: The non-Cartesian FFP Trajectories used in this thesis, all shown here for $N_P = 16$ and identical T_R.

was tested on three separate imaging phantoms: a vasculature phantom, a resolution phantom, and a Derenzo phantom. An FFP scanner with selection field gradients of $(3, 3, -6)$ $T/m/\mu_0$ in the (x, y, z) directions and a drive field amplitude of 30 mT in both x- and y-directions were assumed, corresponding to a FOV of 2×2 cm^2 in the x-y plane. A realistic nanoparticle diameter of 25 nm was assumed [52, 53]. The MPI signal for a single cycle of each trajectory was generated for a fundamental drive field frequency of $f_0 = 25$ kHz with 2.5 MS/s sampling rate. For the Lissajous and bidirectional Cartesian trajectories, $\phi = 0$ was used (see Table 4.1). Before the reconstruction, the signal was filtered using a high pass filter with a cut-off frequency of $1.8 \times f_0$ to completely remove the fundamental harmonic.

4.3 Alternative Reconstructions

The proposed technique was compared with two different x-space-based reconstruction methods to interpolate the given non-Cartesian data onto the Cartesian grid: scattered interpolation and scattered interpolation with trajectory partitioning [54]. In general, scattered interpolation first triangulates the given data using Delaunay triangulation. The vertices of the triangle enclosing each query point (i.e., the grid points) are lifted to obtain the weights corresponding to the data points. Using natural-neighbor interpolation, lifted triangles are then interpolated to obtain the optimal image intensity for the grid point enclosed by the triangle [55].

Using the aforementioned scattered interpolation, two alternative reconstruction techniques were implemented:

1. **Scattered Interpolation**: The data points and the FFP trajectory are directly fed to the interpolation algorithm.

2. **Scattered Interpolation with Partitioning**: The trajectory is partitioned into two non-overlapping segments with nearly orthogonal directions.

Next, an image for each partition is reconstructed using scattered interpolation, and the resulting images are averaged to obtain the final MPI image [54]. The two segments are at approximately 45° and 135° scanning angles for the Lissajous trajectory, and 0° and 90° scanning angles for the bidirectional Cartesian trajectory. Note that this method cannot be applied to the other tested trajectories, as they cannot be partitioned into a few different angles.

These comparison techniques used a fixed grid size of 512×512, independent of the trajectory type and density level.

4.4 Image Quality Analysis

The proposed technique was further analyzed for the Lissajous and the bidirectional Cartesian trajectories at twenty different trajectory density levels between 10 and 200. Note that the density of the data points for an already acquired data can also be artificially altered by upsampling/downsampling the time-domain signal. To test the potential effects of such alterations, the sampled signal for a Lissajous trajectory was spline interpolated/decimated using 9 different sampling factors ranging between 0.25 and 4. This step was performed after the filtering of the fundamental harmonic.

To quantify the effects on image resolution, the FWHM resolution metric was utilized. As dictated by imaging theory [56], the effective FWHM resolution of the reconstructed MPI image, $FWHM_m$, can be approximated as:

$$FWHM_m = \sqrt{FWHM_s^2 + FWHM_k^2} \tag{4.1}$$

Here, $FWHM_s$ is the native resolution of the MPI system, mainly governed by the selection field gradients and nanoparticle properties, and $FWHM_k$ is the FWHM of the gridding kernel as given in Eq. (3.12). The above equation suggests that the effective resolution of the MPI image worsens with increasing kernel width, and the level of resolution loss depends on the relative magnitude of the kernel width with respect to the native resolution. As explained in Section 3.4, the PSF for the Lissajous and bidirectional Cartesian trajectories can be approximated as the isotropic PSF, $h_{iso}(\mathbf{x})$. As there is no closed form expression for the FWHM of $h_{iso}(\mathbf{x})$, it can be computed numerically from a central cross-section of $h_{iso}(\mathbf{x})$. Accordingly, for the parameters used in this thesis, $FWHM_s$ is approximately equal to 2.06 mm.

Next, to quantify the effects of trajectory density and sampling factor on overall image quality, the peak signal-to-noise ratio (PSNR) metric was utilized:

$$PSNR = 10\, log_{10} \left(\frac{\max^2(\rho)}{MSE} \right) \tag{4.2}$$

Here, $\rho(\mathbf{x})$ is the numeric phantom (i.e., the nanoparticle distribution) used in the simulations and MSE is the mean square error between the phantom and the reconstructed image. Here, higher values of PSNR indicate improved image quality.

4.5 Deblurring and Noise Robustness

To show potential improvements in the gridded images, both the equalization filter [48] and Wiener deconvolution methods were implemented for the Lissajous and the bidirectional Cartesian trajectories. As explained in Section 3.4, the equalization filter aims to improve the effective PSF from $h_{iso}(\mathbf{x})$ to $E_T(\mathbf{x})$. For the parameters used in this thesis, this corresponds to an improvement of the effective FWHM from 2.06 mm to 1.47 mm, where the latter is the approximate FWHM of $E_T(\mathbf{x})$ as given in [26]. For Wiener deconvolution, $NSR = 1 \times 10^{-5}$ was utilized.

Prior to performing deblurring via equalization or deconvolution, the reconstructed MPI image was first extended in all four directions by replicating the edges, and the resulting image was gradually faded to zero in the extended regions [57]. After deblurring, the central part of the image was extracted to capture the original FOV. These edge-tapering steps were necessary for avoiding deblurring-induced artifacts at the edges of the FOV.

Noise robustness of the proposed gridding technique and the subsequent deblurring methods were tested at four different signal-to-noise ratio (SNR) levels (50, 20, 10, and 5) using the Lissajous trajectory. White Gaussian noise was added to the simulated signal after the filtering of the fundamental harmonic. Here, SNR was defined as the ratio of the peak signal (after filtering) and the standard deviation of the additive white Gaussian noise.

Chapter 5

Results

5.1 Reconstruction Results and Trajectory Evaluation

Reconstruction results for the proposed algorithm and the comparison techniques can be seen in Figures 5.1 and 5.2 for $N_P = 50$. Figure 5.1 shows the Lissajous and bidirectional Cartesian trajectories, together with the resulting MPI images. The isotropically blurred image, IMG_{iso}, obtained via convolving the phantom with $h_{iso}(\mathbf{x})$ in Eq. (3.14), is also displayed for visual comparison. Note that IMG_{iso} is the MPI image that would be obtained with the standard x-space reconstruction using two orthogonal linear trajectories [35]. As seen in Figure 5.1, directly performing scattered interpolation yields images with abruptly changing pixel intensities. These severe artifacts stem from the fact that the nearby data points on a trajectory can be inconsistent when their scanning directions are different, as the x-space images corresponding to those data points are blurred by distinct PSFs. When data are first partitioned into two non-overlapping segments, the severe artifacts seen in direct scattered interpolation are avoided. However, a closer inspection of these images reveals horizontal and vertical stripe artifacts, which are caused by inconsistencies between the images reconstructed from the

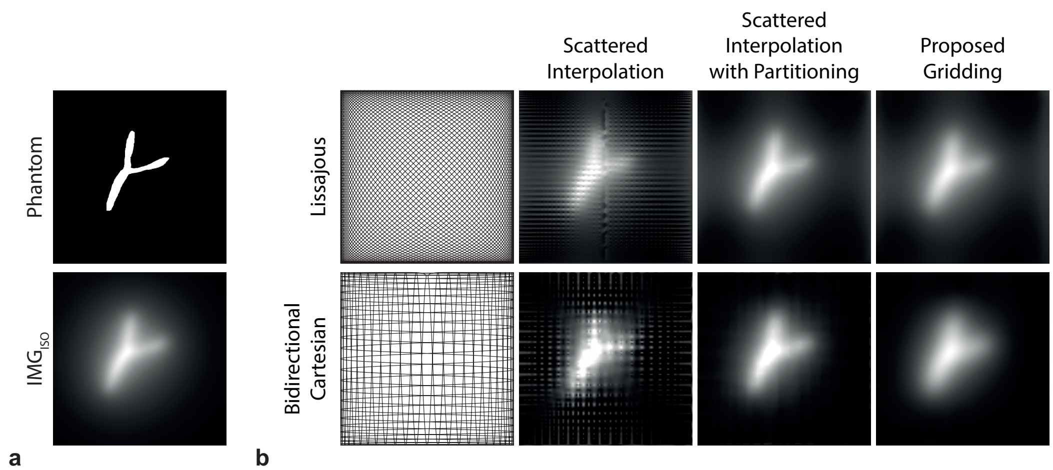

Figure 5.1: Reconstruction results for the Lissajous and bidirectional Cartesian trajectories. **(a)** The phantom and the isotropically blurred image, obtained via convolution with $h_{iso}(\mathbf{x})$ in Eq. (3.14). **(b)** Scattered interpolation causes severe artifacts due to the different scanning directions of nearby data points. While partitioning the data before applying scattered interpolation removes these artifacts, horizontal and vertical stripe artifacts can still be observed. The proposed method does not suffer from any of the aforementioned artifacts, and reconstructs the image by automatically tuning the reconstruction parameters from the scanning trajectory. The results closely match IMG_{iso} for both trajectories. For these simulations, the FOV was 2×2 cm^2 and $N_P = 50$. For each trajectory, the images from all three methods were displayed with identical windowing.

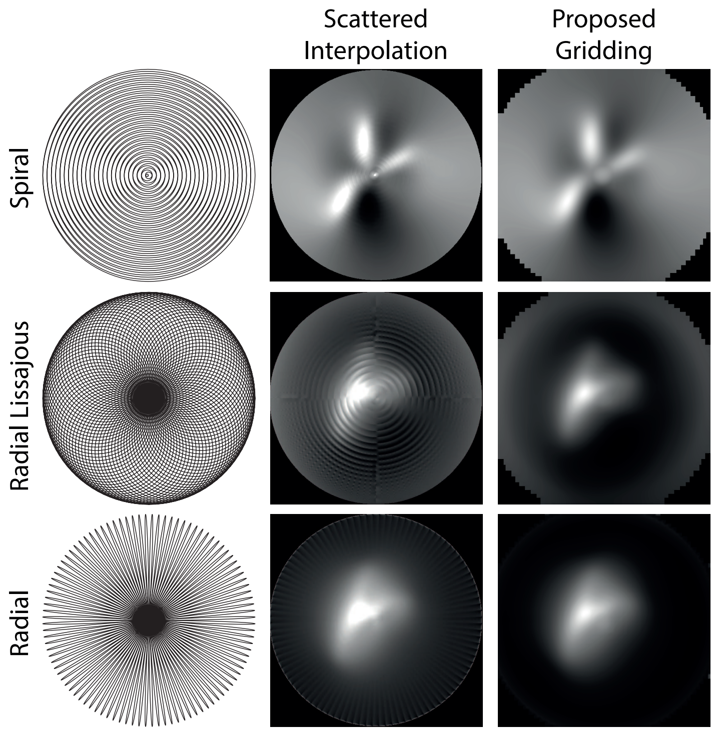

Figure 5.2: Reconstruction results for the trajectories that cannot be partitioned. Images from scattered interpolation have artifacts in the central regions of the images where the trajectories are very dense. Ring-shaped artifacts are observed for the spiral and radial Lissajous trajectories, and streak artifacts are seen for the radial trajectory. The proposed gridding algorithm successfully removes all of these artifacts. However, trajectory-induced smearing results in noticeably blurred MPI images. For these simulations, the FOV was 2×2 cm^2 and $N_P = 50$. For each trajectory, the images from both methods were displayed with identical windowing.

two separate partitions. The proposed gridding algorithm, on the other hand, does not suffer from any of the aforementioned artifacts and reconstructs the x-space MPI image by automatically determining the reconstruction parameters from the MPI data. The resulting images closely match IMG_{iso} for both trajectories. As a trade-off, when compared to the results of scattered interpolation with partitioning, the proposed method induced a slight blurring on the reconstructed images. While this blurring is caused by the interpolation kernel used in gridding, it can be circumvented by appropriate choice of trajectory density and/or sampling factor, as shown in later analyses.

Figure 5.2 shows the reconstructed MPI images for the trajectories that cannot be partitioned, i.e., the spiral, radial Lissajous, and radial trajectories. These trajectories scan the FOV in varying directions, and unlike the Lissajous or bidirectional Cartesian trajectories, they do not feature any main scanning directions. Therefore, the only comparison technique considered here was the direct scattered interpolation method. For the scattered interpolation, the image artifacts occur mostly in the central regions of the images where the trajectories are very dense. Ring-shaped artifacts can be observed for the spiral and radial Lissajous trajectories, whereas the radial trajectory suffers from streak artifacts extending radially from the center of the image. Again, these artifacts stem from inconsistencies among nearby data points. The proposed gridding algorithm successfully removes all of these artifacts. However, the resulting images display noticeable blurring when compared to the results from the Lissajous or bidirectional Cartesian trajectories for the same N_P. Note that the exact same blurring is also present in scattered interpolation results, indicating that it is not caused by the gridding interpolation. It rather reflects a trajectory-induced smearing of the MPI image.

Considering their superior performance, only the Lissajous and bidirectional Cartesian trajectories were considered for subsequent analyses.

5.2 Effects of Trajectory Density

To observe the effects of the trajectory density, N_P, on the quality of the reconstructed images, the signal acquisition process was simulated for four different N_P values: 18, 30, 50, and 98. The resulting images are shown in Figure 5.3a. For the Lissajous trajectory, the vasculature structure can be distinguished even at low density values. For the bidirectional Cartesian trajectory, however, the resolution at very low densities is visibly degraded. Note that the bidirectional Cartesian trajectory is inherently much sparser than the Lissajous trajectory, because the effective trajectory density is reduced by a factor of two to keep the repetition times identical among all trajectories (see the 1/2 factor in Table 4.1 for the frequency ratio of the bidirectional Cartesian trajectory) [29]. For both

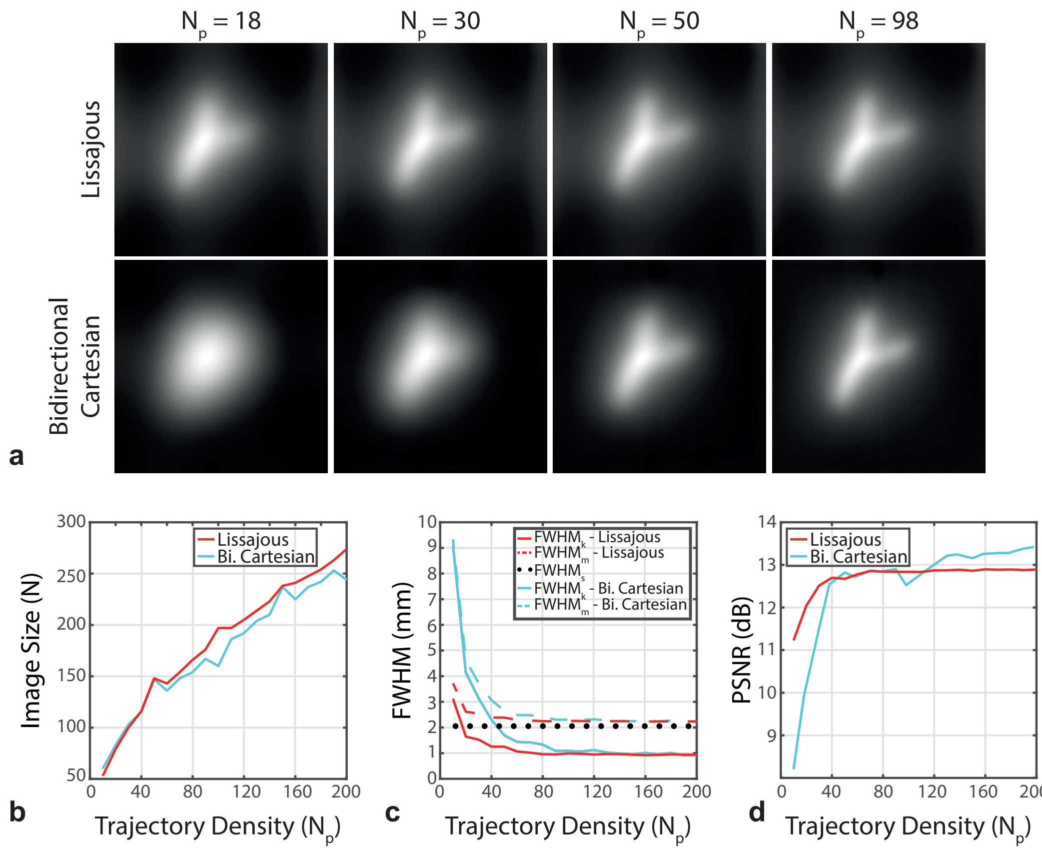

Figure 5.3: The effects of trajectory density, N_P, on the reconstructed MPI images. **(a)** The results of the gridding algorithm for the Lissajous and bidirectional Cartesian trajectories for $N_P = 18$, 30, 50, and 98. As N_P is increased, the resolution of the gridded MPI image improves for both trajectories. **(b)** The image size (N) that is automatically tuned using the MPI trajectory monotonically increases with increasing N_P. **(c)** The FWHM of the gridding kernel decreases and then converges to a constant value as N_P increases. The overall image resolution ($FWHM_m$) also improves and converges to the native resolution of the MPI system ($FWHM_s$) with increasing N_P. **(d)** The overall image quality improves and rapidly converges to a constant PSNR value for both trajectories as N_P increases.

trajectories, as the density of the trajectory is increased, the resolution of the gridded MPI image improves. This effect is quantified in Figures 5.3b and 5.3c, where the automatically computed values for the image size (N) and the effective gridding kernel width (i.e., $FWHM_k$ in Eq. (3.12)) are plotted as functions of N_P, for both the Lissajous and the bidirectional Cartesian trajectories. As expected, N increases with increasing N_P, as the local pixel size dictated by the Voronoi partitions of the data points gets smaller. Furthermore, with increasing N_P, the minimum distance between each grid point and the nearest data point is reduced. This in turn lowers $FWHM_k$ to ensure adequate spread of data points onto nearby grids.

The values for $FWHM_m$ computed using Eq. (4.1) are also plotted in Figure 5.3c. For both trajectories, $FWHM_m$ converges to 2.27 mm for increasing N_P values. Hence, it is deduced that when $FWHM_k$ is sufficiently smaller than $FWHM_s$, the gridding algorithm does not induce any significant blur on the reconstructed images. This criterion is satisfied for $N_P > 50$ for the Lissajous trajectory and for $N_P > 90$ for the bidirectional Cartesian trajectory.

Image quality was also quantified using the PSNR metric, as shown in Figure 5.3d. For both trajectories, image quality sharply increases until N_P reaches 40. Then, PSNR gradually converges to 12.9 dB for the Lissajous trajectory. For the bidirectional Cartesian trajectory, PSNR displays a slowly increasing trend and reaches to 13.4 dB at $N_P = 200$. The bidirectional Cartesian trajectory performs slightly better than the Lissajous trajectory because of its blurring pattern that yields lower image haze in the background. Note that the PSNR value for IMG_{iso} in Figure 5.1a is 12.4 dB. Hence, the quality of the images from the proposed gridded algorithm can exceed those obtained with linear trajectories via standard x-space reconstruction.

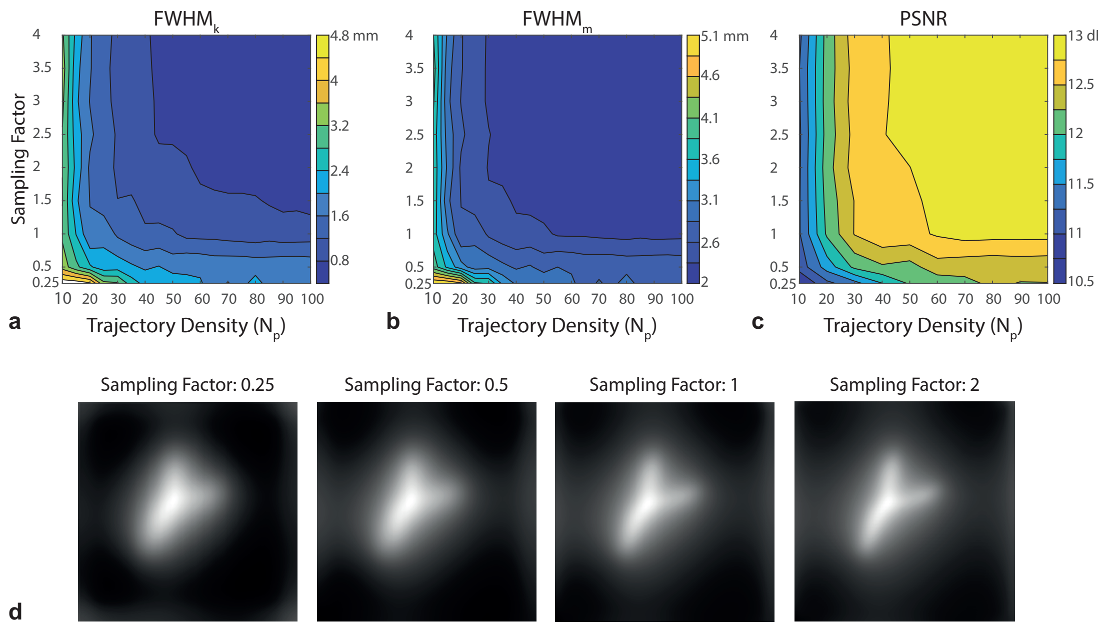

Figure 5.4: Effects of upsampling/downsampling the MPI signal. **(a)** The FWHM of the gridding kernel quickly decreases and **(b)** the overall image resolution converges to the native system resolution for increasing trajectory density and sampling factor. **(c)** The overall image quality also improves with increasing trajectory density and sampling factor, where PSNR converges to 13.0 dB. **(d)** The gridded MPI images at $N_P = 98$ for different sampling factors. A sampling factor of 2 suffices to avoid gridding-induced blurring. For these simulations, the initial sampling rate was 2.5 MS/s.

5.3 Effects of Sampling Factor

In MPI, the density of the data points not only depend on the path of the trajectory, but also on the sampling rate of the signal. Even for a fixed sampling rate, one can artificially alter the density of the data points by upsampling/downsampling the signal. Figure 5.4a shows the FWHM of the gridding kernel as a function of both the trajectory density and the sampling factor, for an initial sampling rate of 2.5 MS/s. Accordingly, for a fixed trajectory density, one can reduce the effective kernel width by upsampling the MPI signal. Figure 5.4b shows the effects of this procedure on the overall resolution of the gridded MPI image. For N_P values greater than approximately 40, upsampling can be utilized to achieve an overall resolution of 2.11 mm, which closely matches the native resolution. In most cases, a sampling factor of 2 is sufficient to avoid any blurring of the MPI image. A similar trend is seen in the PSNR values shown in Figure 5.4c, where PSNR converges to 13.0 dB with a sampling factor of 2 and $N_P > 50$. These results are visually demonstrated in Figure 5.4d, where gridded MPI images at four different sampling factors are displayed for $N_P = 98$. Here, a sampling factor of 2 provides noticeable improvements in image resolution, and suffices to avoid gridding-induced blurring. A sampling factor of 4 does not provide any additional benefits on the image quality.

5.4 Deblurring and Noise Robustness

The resolution of the x-space reconstructed images can be improved via a post-processing step, following gridding. Figure 5.5 illustrates the resolution improvement achieved by applying either an equalization filter or Wiener deconvolution on the gridded images. A 2×2 cm^2 phantom, shown in Figure 5.5a, was utilized to highlight the changes in resolution. Both Lissajous and bidirectional Cartesian trajectories utilized $N_P = 98$. The signal was generated with an initial sampling rate of 2.5 MS/s and upsampled with a sampling factor of 2. As seen in Figure 5.5b, the equalization filter significantly improves the resolution of the image.

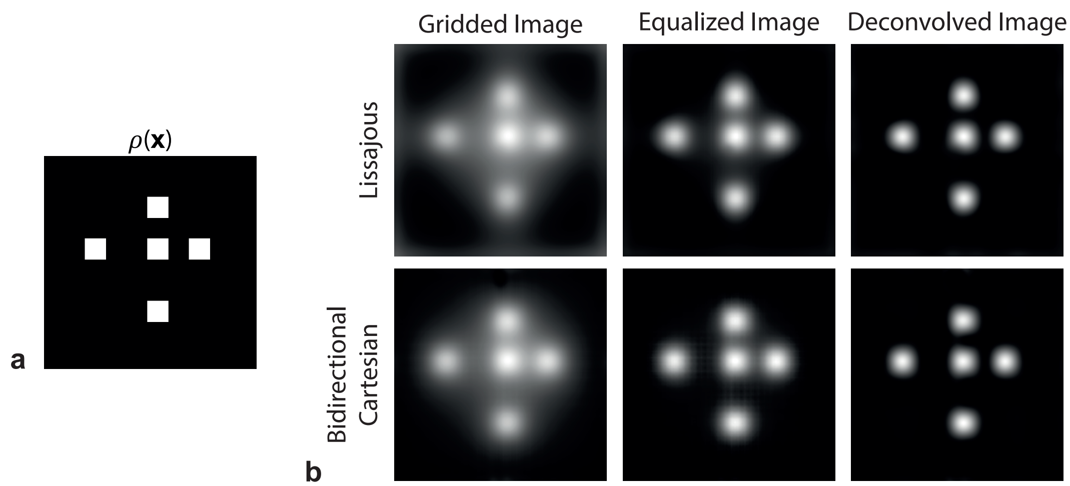

Figure 5.5: Postprocessing results for the proposed gridding algorithm. **(a)** The phantom and **(b)** the results of the gridding algorithm followed by either an equalization filter or Wiener deconvolution. The gridded images can be significantly improved in terms of resolution using either of these two postprocessing techniques. Equalization does not aim to fully deconvolve the effects of the imaging PSF. For these simulations, FOV $= 2 \times 2$ cm^2 and $N_P = 98$, with 2.5 MS/s sampling rate and a sampling factor of 2.

Using Eq. (3.14), for the parameters used in this thesis, this filter aims to improve the effective FWHM from 2.06 mm to 1.47 mm. The deconvolved images in Figure 5.5b show greater improvement in resolution, at the expense of potential noise amplification, as analyzed in detail below. In comparing trajectories, both the equalization and deconvolution techniques gave slightly improved results for the Lissajous trajectories, which is to be expected given the lower effective density of the bidirectional Cartesian trajectory.

Figure 5.6 gives the results for the noise robustness analyses for both the gridding reconstruction and the deblurring techniques. Again, the Lissajous trajectory with $N_P = 98$ was used, and data acquisition was performed at 2.5 MS/s with a sampling factor of 2. For these analyses, a Derenzo phantom was utilized, shown in Figure 5.6a with five resolution levels: 3.9 mm, 3.2 mm, 2.5 mm, 2.0 mm, and 1.4 mm. In the noise free case in Figure 5.6b, the disks that are at 2.5 mm or higher separation are visually resolved in the gridded image. After the equalization filter, the resolution improves visibly and the disks at 2.0 mm

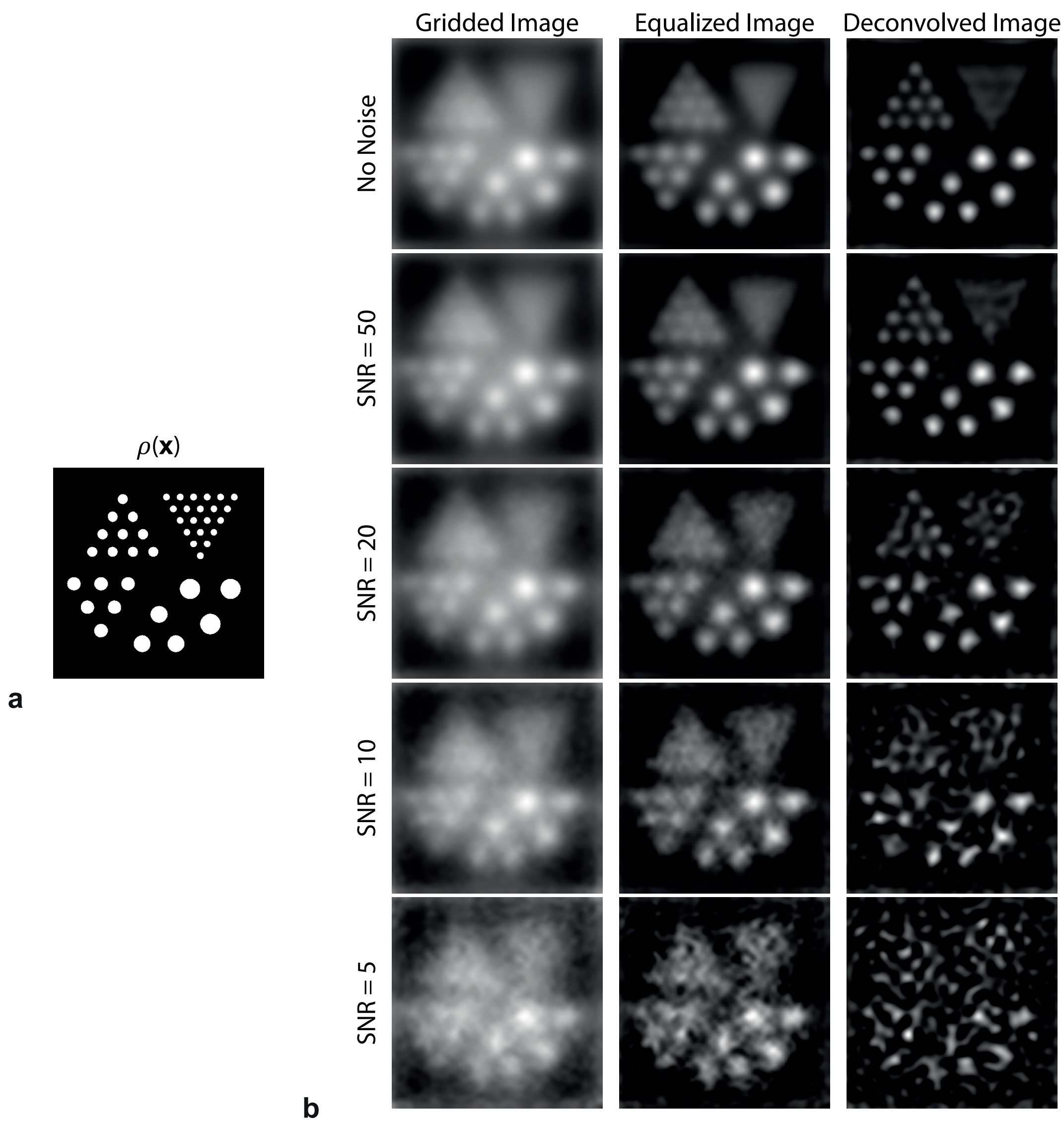

Figure 5.6: Noise robustness results for the proposed gridding algorithm and the postprocessing techniques. **(a)** A Derenzo phantom with five resolution levels: 3.9 mm, 3.2 mm, 2.5 mm, 2.0 mm, and 1.4 mm. **(b)** The gridding algorithm preserves image quality down to SNR levels of 10. Wiener deconvolution yields higher image resolution at high SNR levels, whereas the equalization filter displays improved robustness against artifacts and noise amplification at lower SNR levels. For these simulations, FOV $= 2 \times 2$ cm^2 and $N_P = 98$, with 2.5 MS/s sampling rate and a sampling factor of 2.

separation can also be resolved visually. While Wiener deconvolution further improves the resolution, the disks at 1.4 mm remain unresolved. As seen in Figure 5.6b, the gridding reconstruction shows robustness against noise down to SNR levels of 10. At high SNR levels, Wiener deconvolution yields improved image quality and higher resolution when compared to the equalization filter. At SNR levels around 20 and lower, however, the equalization filter displays improved robustness against artifacts and noise amplification when compared to Wiener deconvolution. The noise amplification in the deconvolved image is clearly visible at SNR = 5, where the background noise competes with image intensity. Note that these results are displayed for a single cycle of the Lissajous trajectory, with a scan time of merely 3.92 ms. Significant improvements in image quality can easily be achieved by increasing the SNR via averaging over multiple cycles.

Chapter 6

Discussion and Conclusion

6.1 Discussion

The proposed gridding algorithm successfully reconstructs MPI images for non-Cartesian trajectories, while automatically computing the reconstruction parameters from the FFP trajectory. Among the tested trajectories, the Lissajous and bidirectional Cartesian trajectories resulted in higher image quality, whereas spiral, radial, and radial Lissajous trajectories yielded excessive blurring. The advantage of the Lissajous and bidirectional Cartesian trajectories is that they are composed of two nearly orthogonal scanning directions. In contrast, spiral, radial, and radial Lissajous trajectories incorporate scanning directions that result in smearing of the MPI image. Note that this result is consistent with earlier work that looked at trajectory analysis for SFR, where the Lissajous and Cartesian trajectories resulted in improved resolution when compared to other trajectories [29]. Hence, it is deduced that the Lissajous and Cartesian trajectories are generally favorable for MPI.

The results demonstrate that the gridded images can be improved via a simple upsampling of the already acquired MPI signal. This simple operation increases the effective trajectory density and helps the proposed method to achieve the native resolution of the MPI system. It should also be noted that directly sampling the signal at 5 MS/s yields visually identical results to sampling at 2.5 MS/s followed by upsampling by a factor of 2 (results not shown). Therefore, considering the fact that the MPI signal quickly fades at higher harmonics, the signal can be sampled at a relatively low rate followed by upsampling, without compromising image quality. In addition, deblurring techniques also help improve the resolution of the reconstructed images. The equalization filter removes the background haze, without noise amplification. Deconvolution, on the other hand, improves the resolution at the expense of significant degradation in SNR. Therefore, especially at realistic SNR levels one may expect to see for *in vivo* imaging, the equalization filter shows a better promise.

The proposed method provides a reconstruction with reduced memory and computational requirements for the trajectories normally utilized with SFR. In SFR, the system matrix contains the calibration data and is of size $(N_f \times N_c \times 2) \times (N \times N)$, where $(N \times N)$ denotes the imaging FOV matrix, N_f is the number of frequency components, N_c is the number of receive coils, and real and imaginary components of the spectrum are stored in separate rows. For a typical scenario with $N = 40$, $N_f = 10000$, $N_c = 2$, approximately 512 MB of memory is needed for the system matrix alone. Meanwhile, the actual imaging data in both the SFR and x-space approaches (including the proposed method) form a vector of length $(N_s \times N_c \times 2)$, where N_s is the number of samples collected in one period of the trajectory (assuming that repeated periods are first averaged). For $N_s = 10000$, approximately 32 MB of memory is needed for the imaging data. Thus, the memory requirement of the x-space approach is substantially smaller than that of the SFR approach ($\sim$32 MB vs. $\sim$544 MB for the given parameters). In terms of computational efficiency, previous studies suggest that algebraic reconstruction technique (ART), which is currently the most popular reconstruction method in SFR, is expected to be of complexity $O(N_f \times N_c \times N_{iter} \times N^2)$, where N_{iter} is the number of iterations [23, 58]. While there have been several efforts to reduce the computational complexity of the SFR approach, the N^2 dependence still remains [59–61]. For the proposed gridding algorithm, on the other hand, the two main steps are the Voronoi partitioning and the gridding operations. Common algorithms for Voronoi partitioning are of complexity $O(N_s \log(N_s))$ [62, 63]. In the gridding stage, the samples on the trajectory are distributed to their nearest grid points. Assuming that $N_g \ll N_s$ samples will be distributed on average to each grid point, this bears a complexity of $O(N_g \times N^2)$ [38]. Hence, the proposed gridding method is advantageous in terms of memory storage, with comparable computational efficiency.

With the abovementioned advantages, the proposed gridding technique is especially promising for real-time imaging applications that require the usage of a rapid scanning trajectory with a rapid image reconstruction method. Trajectories such as the Lissajous trajectory can achieve higher frame rates when compared to line-by-line scanning. In contrast to SFR approaches, the proposed gridding algorithm does not require any calibration scans, and hence can potentially handle arbitrary changes in FOV, trajectory density, nanoparticle type, or nanoparticle environment. These features may especially be valuable for real-time imaging applications where one may need to change the size and/or the position of the FOV on the fly (e.g., during interventional imaging), or where the nanoparticle response may change over time (e.g., due to internalization into a cell environment [19, 64]. For optional deblurring of the reconstructed image, one may need to perform a calibration scan to determine the PSF from a point source phantom. Nevertheless, this procedure takes significantly less time when compared to the calibration of the system matrix. In addition, this technique can enable x-space reconstruction of Lissajous data obtained from existing commercial MPI scanners, which may then facilitate the usage of other x-space-based techniques on those systems (e.g., relaxation-based color MPI [16]).

The results in this thesis assumed that nanoparticle magnetization instantaneously aligns with the applied magnetic field. Nanoparticle relaxation can smear the MPI signal, and hence the image, along the scanning direction. For example, the two dominant directions for the Lissajous trajectory may yield images that are smeared differently. For those cases, one solution can be to perform a low-level correction for relaxation by compensating for relaxation induced signal delays [65]. Alternatively, the effective time constant for relaxation can be estimated from the MPI signal [15, 16], and the underlying adiabatic MPI signal can be recovered via deconvolution [37]. A potential problem that may remain is the position-dependent response of the nanoparticles, which may especially afflict the Lissajous trajectory with its fast field rotation. For such cases, it may be favorable to utilize isotropic nanoparticles with small hydrodynamic diameters, as suggested in [66]. Alternatively, a class of nanoparticles with reduced relaxation effects despite their larger sizes may also be utilized, such as UW33 in [67].

The non-ideality of the magnetic fields may also affect the quality of the reconstructed images. For standard x-space reconstruction, it was previously shown that selection fields with non-homogeneous gradients result in geometric warping of the reconstructed images [68]. These effects are relatively benign and can be successfully corrected using image unwarping techniques, following a measurement and/or computation of the displacement map. Similarly, proposed gridding algorithm is expected to yield images with easily reversible warping in the presence of selection field non-ideality, making it extendable to 3D imaging. Experimental validation of the proposed technique and its extension to 3D remain as important future work.

6.2 Conclusion

In this thesis, a generalized, trajectory-independent, and parameter-free reconstruction algorithm was proposed for x-space MPI. The proposed gridding algorithm automatically tunes gridding kernel width and image size parameters based on the scanning trajectory, without causing any additional blurring of the MPI image. The results demonstrate that the Lissajous and bidirectional Cartesian trajectories are favorable for x-space MPI, as they feature two orthogonal scanning directions that result in an approximately isotropic PSF. The proposed method is especially promising for real-time imaging applications that require rapid scanning trajectories together with a rapid image reconstruction method.

Bibliography

[1] B. Gleich and J. Weizenecker, "Tomographic imaging using the nonlinear response of magnetic particles," *Nature*, vol. 435, no. 7046, pp. 1214–1217, 2005.

[2] J. Weizenecker, J. Borgert, and B. Gleich, "A simulation study on the resolution and sensitivity of magnetic particle imaging.," *Physics in Medicine and Biology*, vol. 52, no. 21, pp. 6363–6374, 2007.

[3] P. W. Goodwill, E. U. Saritas, L. R. Croft, T. N. Kim, K. M. Krishnan, D. V. Schaffer, and S. M. Conolly, "X-space MPI: magnetic nanoparticles for safe medical imaging," *Advanced Materials*, vol. 24, no. 28, pp. 3870–3877, 2012.

[4] E. U. Saritas, P. W. Goodwill, L. R. Croft, J. J. Konkle, K. Lu, B. Zheng, and S. M. Conolly, "Magnetic particle imaging (MPI) for NMR and MRI researchers," *Journal of Magnetic Resonance*, vol. 229, pp. 116–126, 2013.

[5] L. M. Bauer, S. F. Situ, M. A. Griswold, and A. C. S. Samia, "Magnetic particle imaging tracers: state-of-the-art and future directions," *The Journal of Physical Chemistry Letters*, vol. 6, no. 13, pp. 2509–2517, 2015.

[6] J. Weizenecker, B. Gleich, J. Rahmer, H. Dahnke, and J. Borgert, "Three-dimensional real-time in vivo magnetic particle imaging," *Physics in Medicine & Biology*, vol. 54, no. 5, p. L1, 2009.

[7] J. Haegele, J. Rahmer, B. Gleich, C. Bontus, J. Borgert, H. Wojtczyk, T. M. Buzug, J. Barkhausen, and F. M. Vogt, "Visualization of instruments for

cardiovascular intervention using MPI," in *Springer Proceedings in Physics*, vol. 140, pp. 211–215, 2012.

[8] J. Rahmer, D. Wirtz, C. Bontus, J. Borgert, and B. Gleich, "Interactive Magnetic Catheter Steering with 3-D Real-Time Feedback Using Multi-Color Magnetic Particle Imaging," *IEEE Transactions on Medical Imaging*, vol. 36, no. 7, pp. 1449–1456, 2017.

[9] S. Vaalma, J. Rahmer, N. Panagiotopoulos, R. L. Duschka, J. Borgert, J. Barkhausen, F. M. Vogt, and J. Haegele, "Magnetic particle imaging (mpi): experimental quantification of vascular stenosis using stationary stenosis phantoms," *PloS one*, vol. 12, no. 1, p. e0168902, 2017.

[10] J. Salamon, M. Hofmann, C. Jung, M. G. Kaul, F. Werner, K. Them, R. Reimer, P. Nielsen, A. Vom Scheidt, G. Adam, T. Knopp, and H. Ittrich, "Magnetic particle / magnetic resonance imaging: In-vitro MPI-guided real time catheter tracking and 4D angioplasty using a road map and blood pool tracer approach," *PLoS ONE*, vol. 11, no. 6, pp. 1–14, 2016.

[11] A. C. Bakenecker, M. Ahlborg, C. Debbeler, C. Kaethner, T. M. Buzug, and K. Lüdtke-Buzug, "Magnetic particle imaging in vascular medicine," *Innovative Surgical Sciences*, vol. 3, no. 3, pp. 179–192, 2018.

[12] D. Hensley, P. Goodwill, L. Croft, and S. Conolly, "Preliminary experimental x-space color mpi," in *Magnetic particle imaging (IWMPI), 2015 5th international workshop on*, pp. 1–1, IEEE, 2015.

[13] C. Stehning, B. Gleich, and J. Rahmer, "Simultaneous magnetic particle imaging (mpi) and temperature mapping using multi-color mpi," *International Journal on Magnetic Particle Imaging*, vol. 2, no. 2, 2016.

[14] J. Zhong, M. Schilling, and F. Ludwig, "Magnetic nanoparticle temperature imaging with a scanning magnetic particle spectrometer," *Measurement Science and Technology*, vol. 29, no. 11, p. 115903, 2018.

[15] M. Utkur, Y. Muslu, and E. U. Saritas, "Relaxation-based viscosity mapping for magnetic particle imaging," *Physics in Medicine and Biology*, vol. 62, no. 9, p. 3422, 2017.

[16] Y. Muslu, M. Utkur, O. B. Demirel, and E. U. Saritas, "Calibration-free relaxation-based multi-color magnetic particle imaging," *IEEE Transactions on Medical Imaging*, vol. 37, no. 8, pp. 1920–1931, 2018.

[17] M. Moddel, C. Meins, J. Dieckhoff, and T. Knopp, "Viscosity quantification using multi-contrast magnetic particle imaging," *New Journal of Physics*, vol. 20, p. 083001, 2018.

[18] B. Zheng, M. P. Von See, E. Yu, B. Gunel, K. Lu, T. Vazin, D. V. Schaffer, P. W. Goodwill, and S. M. Conolly, "Quantitative magnetic particle imaging monitors the transplantation, biodistribution, and clearance of stem cells in vivo," *Theranostics*, vol. 6, no. 3, pp. 291–301, 2016.

[19] K. Them, J. Salamon, P. Szwargulski, S. Sequeira, M. G. Kaul, C. Lange, H. Ittrich, and T. Knopp, "Increasing the sensitivity for stem cell monitoring in system-function based magnetic particle imaging," *Physics in Medicine and Biology*, vol. 61, no. 9, pp. 3279–3290, 2016.

[20] E. E. Mason, C. Z. Cooley, S. F. Cauley, M. A. Griswold, S. M. Conolly, and L. L. Wald, "Design analysis of an MPI human functional brain scanner," *International Journal on Magnetic Particle Imaging*, vol. 3, no. 1, pp. 1–12, 2017.

[21] J. Rahmer, J. Weizenecker, B. Gleich, and J. Borgert, "Signal encoding in magnetic particle imaging: Properties of the system function," *BMC Medical Imaging*, vol. 9, no. 1, p. 4, 2009.

[22] T. Knopp, T. F. Sattel, S. Biederer, J. Rahmer, J. Weizenecker, B. Gleich, J. Borgert, and T. M. Buzug, "Model-based reconstruction for magnetic particle imaging," *IEEE Transactions on Medical Imaging*, vol. 29, no. 1, pp. 12–18, 2010.

[23] T. Knopp, J. Rahmer, T. Sattel, S. Biederer, J. Weizenecker, B. Gleich, J. Borgert, and T. Buzug, "Weighted iterative reconstruction for magnetic particle imaging," *Physics in Medicine and Biology*, vol. 55, no. 6, p. 1577, 2010.

[24] J. Rahmer, J. Weizenecker, B. Gleich, and J. Borgert, "Analysis of a 3-D system function measured for magnetic particle imaging," *IEEE Transactions on Medical Imaging*, vol. 31, no. 6, pp. 1289–1299, 2012.

[25] P. W. Goodwill and S. M. Conolly, "The X-space formulation of the magnetic particle imaging process: 1-D signal, resolution, bandwidth, SNR, SAR, and magnetostimulation," *IEEE Transactions on Medical Imaging*, vol. 29, no. 11, pp. 1851–1859, 2010.

[26] P. W. Goodwill and S. M. Conolly, "Multidimensional x-space magnetic particle imaging," *IEEE Transactions on Medical Imaging*, vol. 30, no. 9, pp. 1581–1590, 2011.

[27] K. Lu, P. W. Goodwill, E. U. Saritas, B. Zheng, and S. M. Conolly, "Linearity and shift invariance for quantitative magnetic particle imaging," *IEEE Transactions on Medical Imaging*, vol. 32, no. 9, pp. 1565–1575, 2013.

[28] B. Gleich, J. Weizenecker, and J. Borgert, "Experimental results on fast 2D-encoded magnetic particle imaging.," *Physics in Medicine and Biology*, vol. 53, no. 6, pp. N81–N84, 2008.

[29] T. Knopp, S. Biederer, T. Sattel, J. Weizenecker, B. Gleich, J. Borgert, and T. Buzug, "Trajectory analysis for magnetic particle imaging," *Physics in Medicine and Biology*, vol. 54, no. 2, p. 385, 2008.

[30] T. M. Buzug, G. Bringout, M. Erbe, K. Gräfe, M. Graeser, M. Grüttner, A. Halkola, T. F. Sattel, W. Tenner, H. Wojtczyk, *et al.*, "Magnetic particle imaging: Introduction to imaging and hardware realization," *Zeitschrift für Medizinische Physik*, vol. 22, no. 4, pp. 323–334, 2012.

[31] P. W. Goodwill, K. Lu, B. Zheng, and S. M. Conolly, "An x-space magnetic particle imaging scanner," *Review of Scientific Instruments*, vol. 83, no. 3, p. 033708, 2012.

[32] P. Szwargulski, C. Kaethner, M. Ahlborg, and T. Buzug, "A radial lissajous trajectory for magnetic particle imaging," in *Magnetic Particle Imaging (IWMPI), 2015 5th International Workshop on*, pp. 1–1, IEEE, 2015.

[33] F. Werner, N. Gdaniec, and T. Knopp, "First experimental comparison between the Cartesian and the Lissajous trajectory for magnetic particle imaging," *Physics in Medicine and Biology*, vol. 62, no. 9, p. 3407, 2017.

[34] J. J. Konkle, P. W. Goodwill, E. U. Saritas, B. Zheng, K. Lu, and S. M. Conolly, "Twenty-fold acceleration of 3D projection reconstruction MPI," *Biomedizinische Technik/Biomedical Engineering*, vol. 58, no. 6, pp. 565–576, 2013.

[35] K. Lu, P. Goodwill, B. Zheng, and S. Conolly, "Multi-channel acquisition for isotropic resolution in magnetic particle imaging," *IEEE Transactions on Medical Imaging*, vol. 37, no. 9, pp. 1989–1998, 2018.

[36] T. Knopp and T. M. Buzug, *Magnetic particle imaging: an introduction to imaging principles and scanner instrumentation*. Springer Science & Business Media, 2012.

[37] K. Bente, M. Weber, M. Graeser, T. F. Sattel, M. Erbe, and T. M. Buzug, "Electronic field free line rotation and relaxation deconvolution in magnetic particle imaging," *IEEE Transactions on Medical Imaging*, vol. 34, no. 12, pp. 644–651, 2015.

[38] J. D. O'Sullivan, "A Fast Sinc Function Gridding Algorithm for Fourier Inversion in Computer Tomography," *IEEE Transactions on Medical Imaging*, vol. 4, no. 4, pp. 200–207, 1985.

[39] H. Schomberg and J. Timmer, "The Gridding Method for Image Reconstruction by Fourier Transformation," *IEEE Transactions on Medical Imaging*, vol. 14, no. 3, pp. 596–607, 1995.

[40] G. H. Glover and J. M. Pauly, "Projection Reconstruction Techniques for Reduction of Motion Effects in MRI," *Magnetic Resonance in Medicine*, vol. 28, no. 2, pp. 275–289, 1992.

[41] J. R. Liao, J. M. Pauly, T. J. Brosnan, and N. J. Pelc, "Reduction of motion artifacts in cine MRI using variable-density spiral trajectories," *Magnetic Resonance in Medicine*, vol. 37, no. 4, pp. 569–575, 1997.

[42] A. Macovski, “Volumetric NMR imaging with time-varying gradients,” *Magnetic Resonance in Medicine*, vol. 2, no. 1, pp. 29–40, 1985.

[43] S. J. Norton, “Fast magnetic resonance imaging with simultaneously oscillating and rotating fiell gradients,” *IEEE Transactions on Medical Imaging*, vol. 6, no. 1, pp. 21–31, 1987.

[44] J. I. Jackson, C. H. Meyer, D. G. Nishimura, and A. Macovski, “Selection of a Convolution Function for Fourier Inversion Using Gridding,” *IEEE Transactions on Medical Imaging*, vol. 10, no. 3, pp. 473–478, 1991.

[45] P. J. Beatty, D. G. Nishimura, and J. M. Pauly, “Rapid gridding reconstruction with a minimal oversampling ratio,” *IEEE Transactions on Medical Imaging*, vol. 24, no. 6, pp. 799–808, 2005.

[46] V. Rasche, R. Proksa, R. Sinkus, P. Börnert, and H. Eggers, “Resampling of data between arbitrary grids using convolution interpolation,” *IEEE Transactions on Medical Imaging*, vol. 18, no. 5, pp. 385–392, 1999.

[47] C. Kaethner, W. Erb, M. Ahlborg, P. Szwargulski, T. Knopp, and T. M. Buzug, “Non-equispaced system matrix acquisition for magnetic particle imaging based on lissajous node points,” *IEEE transactions on medical imaging*, vol. 35, no. 11, pp. 2476–2485, 2016.

[48] K. Lu, P. Goodwill, B. Zheng, and S. Conolly, “Reshaping the 2D MPI PSF to be isotropic and sharp using vector acquisition and equalization,” in *Magnetic Particle Imaging (IWMPI), 2015 5th International Workshop on*, pp. 1–1, IEEE, 2015.

[49] K. Lu, *Linearity, Shift-Invariance and Resolution Improvement for Quantitative Magnetic Particle Imaging.* PhD thesis, UC Berkeley, 2015.

[50] K. Lu, B. Zheng, J. Konkle, E. Saritas, P. Goodwill, and S. Conolly, “Towards multidimensional x-space magnetic particle imaging for improved resolution,” in *Magnetic Particle Imaging (IWMPI), 2013 International Workshop on*, pp. 1–1, IEEE, 2013.

[51] P. Goodwill, *Narrowband and x-space magnetic particle imaging*. PhD thesis, UC Berkeley, 2010.

[52] R. M. Ferguson, A. P. Khandhar, S. J. Kemp, H. Arami, E. U. Saritas, L. R. Croft, J. Konkle, P. W. Goodwill, A. Halkola, J. Rahmer, J. Borgert, S. M. Conolly, and K. M. Krishnan, "Magnetic particle imaging with tailored iron oxide nanoparticle tracers," *IEEE Transactions on Medical Imaging*, vol. 34, no. 5, pp. 1077–1084, 2015.

[53] M. G. Kaul, T. Mummert, C. Jung, J. Salamon, A. P. Khandhar, R. M. Ferguson, S. J. Kemp, H. Ittrich, K. M. Krishnan, G. Adam, *et al.*, "In vitro and in vivo comparison of a tailored magnetic particle imaging blood pool tracer with resovist," *Physics in Medicine & Biology*, vol. 62, no. 9, p. 3454, 2017.

[54] A. Alacaoglu, A. A. Ozaslan, and E. U. Saritas, "Nonlinear Scanning in X-Space MPI," in *International Workshop on Magnetic Particle Imaging (IWMPI) 2016, Book of Abstracts*, p. 74, 2016.

[55] I. Amidror, "Scattered data interpolation methods for electronic imaging systems: a survey," *Journal of Electronic Imaging*, vol. 11, no. 2, pp. 157–177, 2002.

[56] J. L. Prince and J. M. Links, *Medical imaging signals and systems*. Pearson Prentice Hall Upper Saddle River, NJ, 2006.

[57] O. Yorulmaz, O. B. Demirel, T. Çukur, E. U. Saritas, and A. E. Çetin, "A Blind Deconvolution Technique Based on Projection Onto Convex Sets for Magnetic Particle Imaging," pp. 1–19, 2017.

[58] S. Li, C. Chan, J. P. Stockmann, H. Tagare, G. Adluru, L. K. Tam, G. Galiana, R. T. Constable, S. Kozerke, and D. C. Peters, "Algebraic reconstruction technique for parallel imaging reconstruction of undersampled radial data: application to cardiac cine," *Magnetic Resonance in Medicine*, vol. 73, no. 4, pp. 1643–1653, 2015.

[59] T. Knopp and M. Hofmann, "Online reconstruction of 3d magnetic particle imaging data," *Physics in Medicine & Biology*, vol. 61, no. 11, p. N257, 2016.

[60] L. Schmiester, M. Möddel, W. Erb, and T. Knopp, "Direct image reconstruction of lissajous-type magnetic particle imaging data using chebyshev-based matrix compression," *IEEE Transactions on Computational Imaging*, vol. 3, no. 4, pp. 671–681, 2017.

[61] T. Kluth and B. Jin, "Enhanced reconstruction in magnetic particle imaging by whitening and randomized svd approximation," *Physics in Medicine & Biology*, vol. 64, no. 12, p. 125026, 2019.

[62] G. Leach, "Improving worst-case optimal delaunay triangulation algorithms," in *In 4th Canadian Conference on Computational Geometry*, p. 15, 1992.

[63] H. Edelsbrunner and N. R. Shah, "Incremental topological flipping works for regular triangulations," *Algorithmica*, vol. 15, no. 3, pp. 223–241, 1996.

[64] B. Zheng, T. Vazin, P. W. Goodwill, A. Conway, A. Verma, E. U. Saritas, D. Schaffer, and S. M. Conolly, "Magnetic particle imaging tracks the long-term fate of in vivo neural cell implants with high image contrast," *Scientific Reports*, vol. 5, p. 14055, 2015.

[65] L. R. Croft, P. W. Goodwill, and S. M. Conolly, "Relaxation in x-space magnetic particle imaging," *IEEE Transactions on Medical Imaging*, vol. 31, no. 12, pp. 2335–2342, 2012.

[66] M. Graeser, K. Bente, A. Neumann, and T. Buzug, "Trajectory dependent particle response for anisotropic mono domain particles in magnetic particle imaging," *Journal of Physics D: Applied Physics*, vol. 49, no. 4, p. 045007, 2015.

[67] L. R. Croft, P. W. Goodwill, J. Konkle, H. Arami, D. A. Price, A. X. Li, E. U. Saritas, and S. M. Conolly, "Low drive field amplitude for improved image resolution in magnetic particle imaging," *Medical Physics*, vol. 43, no. 1, pp. 424–435, 2016.

[68] E. Yagiz, M. Utkur, O. C. Eren, and E. U. Saritas, "Selection-Field-Induced Warping in X-Space MPI," in *International Workshop on Magnetic Particle Imaging (IWMPI) 2019, Book of Abstracts*, p. 74, 2019.

Appendix A

Decomposition of MPI PSF into Tangential and Normal Envelopes

To simplify the derivation of Equation 2.19, the following definitions are presented [26]:

$$\mathbf{r} \triangleq \frac{\mathbf{G}\left(\mathbf{x_s}(t) - \mathbf{x}\right)}{H_{sat}} \tag{A.1}$$

$$\dot{\mathbf{r}} = \frac{\mathbf{G}\dot{\mathbf{x}}_{\mathbf{s}}(t)}{H_{sat}} \tag{A.2}$$

$$\hat{\mathbf{r}} \triangleq \frac{\mathbf{r}}{\|\mathbf{r}\|} \tag{A.3}$$

$$\hat{\mathbf{r}} = \frac{\dot{\mathbf{r}}}{\|\mathbf{r}\|} + \frac{\dot{\mathbf{r}}^T\mathbf{r}}{\|\mathbf{r}\|^3} \tag{A.4}$$

where $\dot{\mathbf{r}}$ can be decomposed into :

$$\dot{\mathbf{r}} = \dot{\mathbf{r}}_{\|} + \dot{\mathbf{r}}_{\perp} \tag{A.5}$$

where $\dot{\mathbf{r}}_{\|}$ denotes the tangential component and $\dot{\mathbf{r}}_{\perp}$ denotes the normal component.

$$\dot{\mathbf{r}}_{\|} = (\dot{\mathbf{r}} \cdot \hat{\mathbf{r}})\hat{\mathbf{r}} = \left(\dot{\mathbf{r}} \cdot \frac{\mathbf{r}}{\|\mathbf{r}\|}\right)\hat{\mathbf{r}} \tag{A.6}$$

$$\dot{\mathbf{r}}_{\perp} = \left[\dot{\mathbf{r}} - \left(\dot{\mathbf{r}} \cdot \frac{\mathbf{r}}{\|\mathbf{r}\|}\right)\hat{\mathbf{r}}\right] \tag{A.7}$$

Using these decompositions, the derivative of the Langevin function can be defined as follows [26]:

$$\frac{d}{dt}\mathcal{L}(\|\mathbf{r}\|)\hat{\mathbf{r}} = \dot{\mathcal{L}}(\|\mathbf{r}\|)\dot{\mathbf{r}}_{\|} + \frac{\mathcal{L}(\|\mathbf{r}\|)}{\|\mathbf{r}\|}\mathbf{r}_{\perp} \tag{A.8}$$

Using the derivation in A.8, the following multidimensional signal equation can be obtained [26]:

$$s(t) = \frac{d}{dt}\iiint \mathbf{B_1}(\mathbf{u})m\rho(\mathbf{u})\mathcal{L}(\|\mathbf{r}\|)\hat{\mathbf{r}}d\mathbf{u} \tag{A.9}$$

$$= \iiint \mathbf{B_1}(\mathbf{u})m\rho(\mathbf{u})\left[\mathcal{L}(\|\mathbf{r}\|)\dot{\mathbf{r}}_{\|} + \frac{\mathcal{L}(\|\mathbf{r}\|)}{\|\mathbf{r}\|}\dot{\mathbf{r}}_{\perp}\right]d\mathbf{u} \tag{A.10}$$